THE ASTROPHYSICAL JOURNAL SUPPLEMENT SERIES, 75:877–904, 1991 March

BOK GLOBULES AND SMALL MOLECULAR CLOUDS: DEEP *IRAS* PHOTOMETRY AND ^{12}CO SPECTROSCOPY

DAN P. CLEMENS,[1,2] JOÃO LIN YUN,[1] AND MARK H. HEYER[3,4]
Received 1990 January 25; accepted 1990 July 20

ABSTRACT

The sample of 248 small molecular clouds (mostly Bok globules) cataloged by Clemens and Barvainis has been probed using deep, co-added *IRAS* image analysis and via millimeter-wavelength ^{12}CO spectroscopy. Co-adding of the *IRAS* data lowered the flux limits of all four *IRAS* bands to far below the detection thresholds for these clouds: virtually all of the clouds were detected in all four *IRAS* bands. The ^{12}CO spectroscopy revealed 244 (98%) detections, verifying the molecular nature of these clouds. In this paper the *IRAS* co-added fluxes and ^{12}CO $J = 2-1$ line parameters are presented. Our characterization of these Bok globules has revealed mean *IRAS* flux ratios (colors) of 0.70 for log (S_{100}/S_{60}), 0.68 for log (S_{60}/S_{25}), and 0.01 for log (S_{25}/S_{12}). These *IRAS* flux ratio distributions indicate average dust temperatures of 26±5 K for the 60 and 100 μm bands, 71±16 K for the 25 and 60 μm bands, and 254±72 K for the 12 and 25 μm bands. The average broad-band *IRAS* spectrum for this sample of clouds shows the 12 μm excess emission usually associated with small, warm, nonequilibrium grains in the cloud peripheries. The *IRAS* colors are virtually identical to those of other molecular clouds in our Galaxy. Hence, the *IRAS* data base cannot be used to select Bok globules based on their locations in color-color diagrams.

For an assumed sample distance of 600 pc, the mean L_{FIR} is about 6 $L_\odot$, which is close to the value expected of clouds externally heated by the interstellar radiation field. Similarly, using crude assumptions about the cloud structures, the CO observations were used to estimate mean cloud masses of about 11 $M_\odot$. The mean L_{FIR}/M_{H_2} for this cloud sample is 0.5 $L_\odot/M_\odot$, much smaller than the mean of about 3 $L_\odot/M_\odot$ typical of the Galactic disk. We found only a mild correlation between integrated ^{12}CO emission and cloud-averaged dust optical depth for these clouds.

Extrapolating our findings to the entire Galaxy, we estimate the total number of Bok globules to be around 3.2×10^5. The total mass of these clouds is roughly 3.5×10^6 $M_\odot$, representing approximately 0.1% of the Galaxy molecular mass. The total FIR luminosity of Bok globules in the Galaxy is about 2×10^6 $L_\odot$, roughly 0.014% of the total FIR luminosity of the Galaxy.

Subject headings: infrared: sources — interstellar: molecules — nebulae: general — photometry

I. INTRODUCTION

What are the physical conditions which exist in molecular clouds just prior to the onset of star formation? The answer to this question will play an important role in our understanding of star and planet formation (Boss 1989). In an attempt to answer the question, we are investigating the star-forming properties of the smallest and simplest of the molecular clouds, the small Bok globules. The structures of these clouds are much simpler than the larger Giant Molecular Clouds, and multiple bursts or multiple sites of star formation do not seem to be a concern for the globules. Star formation does occur in some of these clouds (Keene *et al.* 1983; Beichman *et al.* 1984), though others appear to be extremely stable (Dickman and Clemens 1983).

Previous studies of Bok globules (e.g., Leung, Kutner, and Mead 1982) used the list of objects generated by Barnard (1927), which tend to be larger (>10′) and thereby fairly massive clouds ($M > 10^{2-3}$ $M_\odot$). In a previous paper (Clemens and Barvainis 1988, hereafter CB), a list of 248 small (mean size ~ 4′) molecular clouds was presented. The far-infrared properties of these clouds were determined through positional association with the *IRAS* Point Source Catalog (PSC). The PSC flux limit of 3 Jy at 100 μm and 1 Jy at 60 μm resulted in most of the small clouds being missed in the association process. However, from the log (N)–log (S_{100}) distribution, a prediction of near 100% detection for co-added *IRAS* data processing was made.

In this paper, we present the results of an analysis of co-added *IRAS* images of the entire sample of 248 CB clouds. The analysis consisted of performing positionally matched aperture photometry at the four *IRAS* wavelengths using the co-added images. As the shorter wavelength (12, 25 μm) emission was generally weak within the globule apertures, we chose to analyze the higher signal-to-noise aperture integrated fluxes for the current study. Analysis of the subset of the CB globule sample with stronger, and thereby resolvable, short-wavelength emission is the subject of future papers. The detection rate of CB globules within the apertures selected was nearly 100%, as predicted, in all four *IRAS* bands. We also present the results of a ^{12}CO $J = 2-1$ survey of the central positions of 247 of the CB clouds.

Analysis of these new data sets allowed rough characterization of the mean *IRAS* luminosities, CO traced molecular masses, and the ratio of L/M for these Bok globules. For the Bok globule class of molecular clouds, the analysis confirmed earlier observations (Keene *et al.* 1980) of single globules

[1] Astronomy Department, Boston University.
[2] Guest Observer, Millimeter Wave Observatory, University of Texas.
[3] Department of Astronomy and Astrophysics, University of Pennsylvania.
[4] Department of Terrestrial Magnetism, Carnegie Institution of Washington.

which showed that the chief source of energy input to these clouds was the interstellar radiation field.

In the following section, our method of co-added image analysis is presented, followed by a discussion of the data collection parameters for the ^{12}CO survey. In § III, we present the combined *IRAS* and CO data set for all of the CB clouds and the histograms of mean properties. In § IV we attempt to use these mean properties to explore aspects of the globule population and to comment on star formation in these clouds. Section V summarizes our findings in detail.

II. DATA COLLECTION AND ANALYSIS

a) Co-Added IRAS Image Analysis

The process of obtaining co-added *IRAS* photometry involved field selection, background estimation, source identification, and matched aperture photometry. A total of 187 1° × 1° fields were selected for co-addition of the *IRAS* survey data. The field centers were chosen to be either between the multiple CB clouds appearing in the fields, or, in the case of single cloud fields, to coincide with the CB cloud position. Field sizes of 1° × 1° were chosen as a compromise between being large enough for easy globule and background identification and being small enough to be processed into co-added form easily.

At the Image Processing and Analysis Center (IPAC),[5] the 60 and 100 μm co-added images were pixel replicated (expanded) so that all four bands were represented with identical sized pixels and images. The final pixel sizes were 0.′25 × 0.′25, with the 60 μm images having been expanded from 0.′5 original resolution, and the 100 μm images from 1′ original resolution. Each image was examined, and large constant or sloping background levels were removed interactively through planar fitting.

Selection of the background photometry apertures was performed typically while viewing the 100 μm image for a field. The background apertures were chosen to be at least as large as the source apertures and to miss all bright sources and most weak sources. As such, each background aperture was a fairly complex shaped polygon.

Selection of the source apertures was guided in one of two ways. If the 100 μm images showed a prominent source of emission coincident with the CB cataloged cloud position, then the observed structure was delineated to form an aperture out to locations where the emission fell to near the background value. For fields where no prominent 100 μm emission was found at the cataloged positions of the clouds, an aperture was selected whose position, size, and orientation mimicked the optically determined cloud extent, but with an *IRAS* appropriate aperture typically 2–3 times larger than the optical size to take into account the poorer 100 μm spatial resolution of *IRAS*. In some cases the *IRAS* image showed an apparent CB cloud connected to a larger structure. In these cases, the source aperture was truncated based on the optical shape and size of the CB cloud. That is, the larger nonglobule cloud was not included in the source aperture. In cases where two or more CB clouds exhibited overlapping *IRAS* emission, the apertures were chosen to assign the observed emission to the respective clouds based on the relative ratios of their optically cataloged sizes.

Analysis of an image consisted of removing constant or sloping backgrounds, measurement of the integrated flux in the source aperture, and measurement of the integrated flux and rms scatter in the background aperture. Each of the four *IRAS* band images for a frame was identically processed, including using the identical source and background apertures. This had the effect of using matched apertures for all four *IRAS* bands. Such was not the case for the PSC, whose point source template sizes changed with the band. For true point sources, this difference is unimportant. However, these small Bok globules are somewhat extended with respect to the PSC templates. Nonmatched apertures would therefore introduce a color shift to the derived fluxes of these extended sources. Matched apertures introduce no such shift and can be chosen to collect all of the emitted flux from the sources.

On a more subtle note, the matched aperture photometry carries none of the "point source" connotation of the PSC. Many authors have confused the appearance of a PSC entry with the existence of an embedded nonvisible star. The PSC "detected" many of the CB globules not because of any embedded star (the co-added images are clear on this point), but because the CB clouds are small compared to the point source templates at 60 and 100 μm.

As an example of the source apertures selected, Figure 1 presents a collection of four frames, with the optically cataloged CB positions, extents, and orientations indicated by the enclosed ellipses, and the selected source apertures by the enclosing polygons. The 100 μm intensity is displayed as grayscale maps for each field.

A comparison of the PSC fluxes and our co-added fluxes for the globules with PSC detections is indicated in Figure 2. There the histograms of the log of the flux ratios in each band are shown. A summary of the figure is that, on average, the PSC missed around 75% of the flux from these clouds. The degree of variation is least for the 100 μm band and somewhat larger for the other three bands. If one were trying to estimate the efficiency these clouds exhibit for reradiation of the interstellar radiation field into the far-infrared, use of the PSC fluxes would lead to erroneous conclusions.

The final values of the sources fluxes were obtained by differencing the values of integrated flux of the source and background apertures. Two estimates of the uncertainties of these globule fluxes were also computed. The first estimate was computed from the dispersion of the pixel-to-pixel flux values within each background aperture. This tended to give low values for the uncertainty. The second method consisted of using the dispersion of pixel fluxes obtained for 20–30 positions across the image chosen to sample the background of disconnected regions (the background aperture sampled only one simply connected region). This latter dispersion tended to be larger than the first dispersion. Hence, to better estimate systematic and random uncertainties, we adopted the larger dispersion, scaling it to account for the variation in flux expected for an aperture the size of the source aperture. In Table 1, the source fluxes and uncertainties are listed for all four bands, as are the areas of the source apertures (in square arcmin). The first column of Table 1 lists the cloud number as found in CB.

[5] IPAC is funded by NASA as part of the *IRAS* extended mission program under contract to JPL.

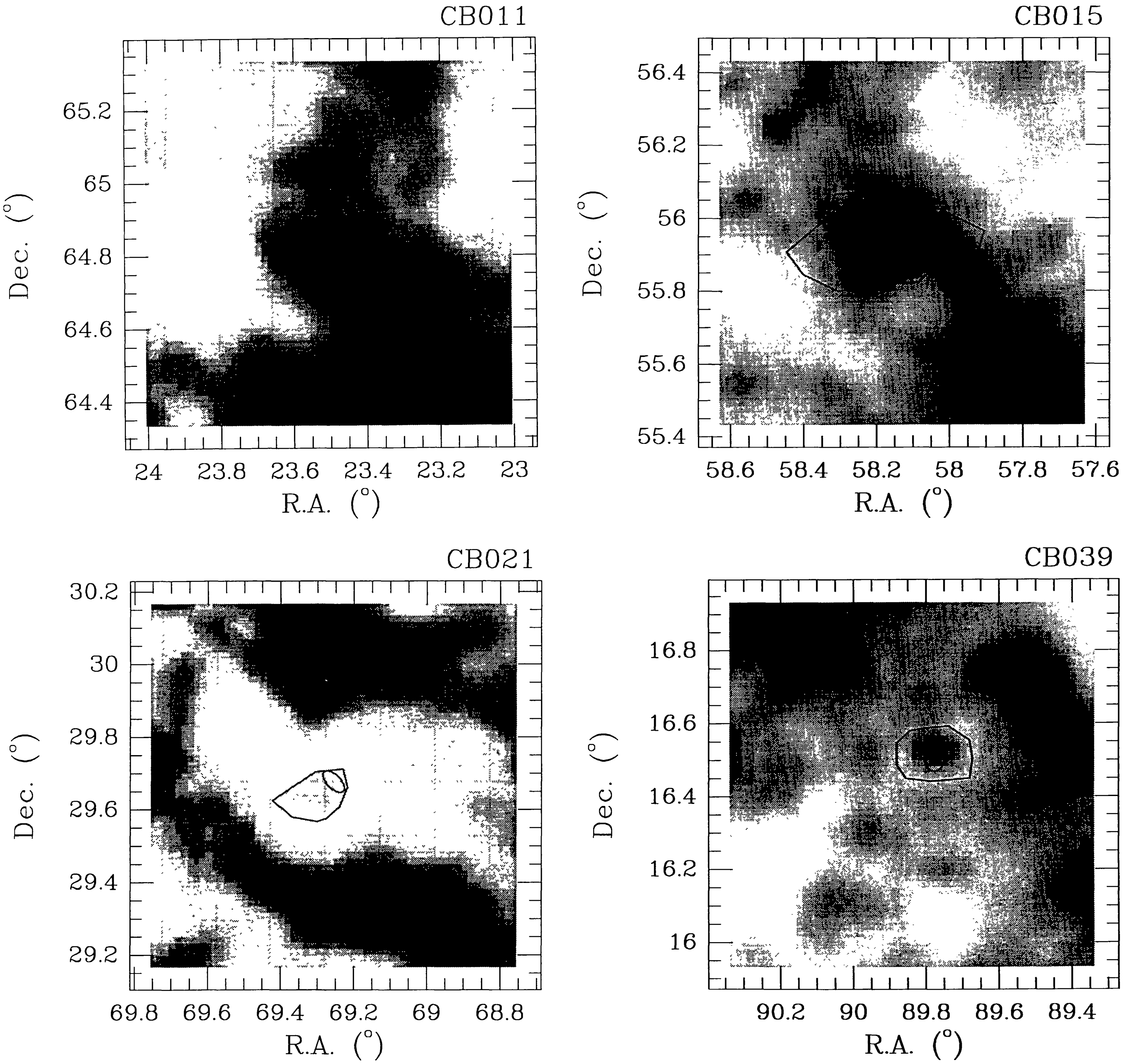

FIG. 1.—Sample of four co-added *IRAS* 100 μm image frames showing the CB optically cataloged cloud orientations and extents (*ellipses*) and source apertures chosen for integration of the *IRAS* emission (*polygons*). In general, although the globules were not always the brightest sources in the frames, their identification was straightforward.

The next four columns list the net flux and uncertainty for each *IRAS* band. A very small number of the clouds show net negative fluxes (9% at 12 μm, 4% at 25 μm, 3% at 60 μm, and 1% at 100 μm). While viewing a few of these images, it became apparent that *absorption* or *scattering* of the short-wavelength radiation (12 μm) was occurring, typically by a globule projected against a bright background source of extended emission. In Figure 3, the 12 μm co-added *IRAS* image for the field including CB 181 (B134) is shown. In that figure, the ellipse corresponds to the optically cataloged globule position. At that position, the 12 μm emission level is *below* the emission level just outside the ellipse. We interpret this emission distribution to consist of bright background 12 μm emission with absorbing or scattering occurring within the foreground globule. In other frames, source crowding and other background problems were clearly affecting the quality of the derived photometry. Hence, although the uncertainties listed are estimates based on the background fluctuations, they may underestimate any system-

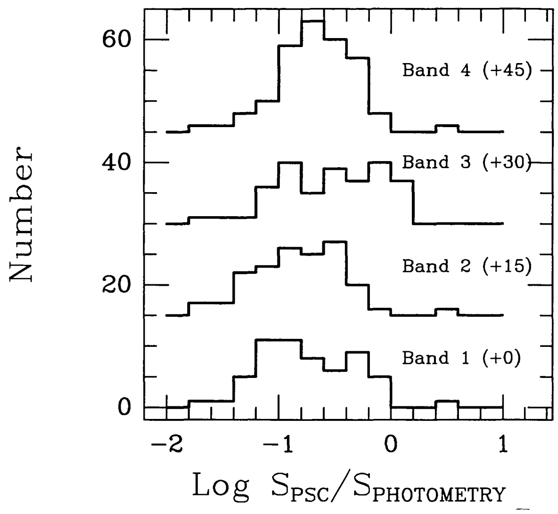

FIG. 2.—Comparison of the fluxes reported for the CB clouds in the *IRAS* PSC and the fluxes found here using the matched aperture photometry, binned by *IRAS* band. The horizontal axis is the log of the flux ratio in each band, as the ratio of the PSC flux to the matched aperture ("photometry") flux. The mean ratio is around −0.6, implying that the PSC missed around 75% of the flux in each band.

atic effects present. The negative fluxes were therefore retained to indicate which clouds have fluxes which are more uncertain than usual. For calculations of luminosities and flux ratios, these negative fluxes were replaced with 3 σ upper limits.

b) CO *Observations*

The ^{12}CO ($J = 2 - 1$, $\lambda = 1.3$ mm) observations were obtained at the Millimeter Wave Observatory[6] on Mount Locke, near Fort Davis, Texas, during 1987 April 17–26 and 1988 March 11–21, as described by CB. The telescope main beam efficiency of 0.66 and beam size at 230 GHz of 66″ were obtained from continuum scans of Jupiter, Saturn, and Venus. Individual spectra were calibrated using the chopper wheel method and from frequent sky tips to determine the atmospheric opacity. During the 1987 observing, the mean sky opacity was around 0.4, while the corresponding 1988 value was 0.15. For all observations, frequency-switched spectra of 2–5 minute duration were obtained in a 256 × 250 kHz filter bank. The positions observed for each cloud were those cataloged by CB. These generally correspond to the central portions of the small clouds.

Almost all of the spectra showed single lines, which were presumed to arise in the gas contained in the CB cloud along the line of sight. For instances of multiple lines, position-switched spectra were obtained, with the reference positions initially 10′ north of the globule position. Reference positions were successively tried around the cloud until no contamination from other clouds was found.

The resulting spectra were baselined, folded (for the frequency-switched spectra), and fitted using a single Gaussian. Columns (7), (8), and (9) of Table 1 list the results of the Gaussian fits to the lines. The temperature listed corresponds to the observed antenna temperature corrected for the main beam efficiency. In that table, in the notes column, an "N" indicates a spectrum with a very narrow CO line (generally spanning only two channels), signifying that the Gaussian fitting was somewhat underdetermined (16% of the clouds). An "F" indicates a line which is unusually wide or flat-topped (5%), and a "D" indicates a line which is doubled (8%), for example by self-absorption. A visual estimate of the quality of the Gaussian fitting is given by the numbers in the notes column. A "1" indicates an excellent fit (49% of the clouds), one where the line is clearly well-represented by a Gaussian. A "2" indicates that the Gaussian is a good approximation to the line (36%), and a "3" signifies that the Gaussian fitting does not adequately describe the line shape or that the spectrum was unusually noisy (15%). Figure 4 shows examples of some of the different spectral categories noted.

In all, 247 clouds were successfully observed in ^{12}CO, with three clouds showing no CO to extremely low levels. Either the CO abundances in these clouds are abnormally low (e.g., CB 61), as has been shown for some high-latitude clouds (Blitz *et al.* 1990), or the presence of the clouds in the CB catalog is spurious (e.g., CB 53, CB 62). Several of the detected clouds were mapped using narrower filters (62.5 kHz) at ^{12}CO and ^{13}CO, and their cores were observed at $C^{18}O$. The ^{12}CO line parameters for these clouds have been included in Table 1; the maps will be presented in later papers.

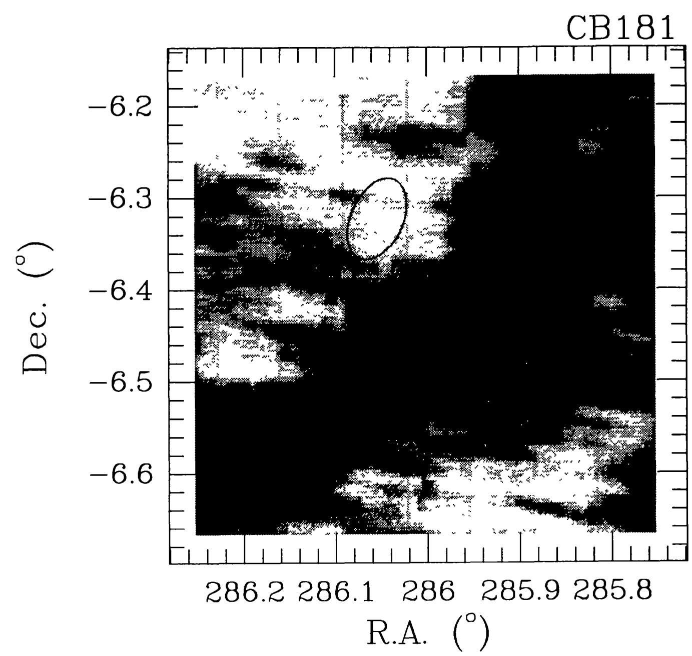

FIG. 3.—*IRAS* co-added 12 μm survey image of the 0°.5 × 0°.5 field including CB 181 (B134). The ellipse indicates the optically cataloged position and approximate extent of the opaque core of the globule. In this image, the 12 μm intensity toward the globule is lower than the intensity outside the globule. For aperture photometric analysis, subtraction of a nearby background aperture flux from the ellipse aperture flux would produce a net negative 12 μm flux. From the distribution of 12 μm emission in this frame, we believe the globule is projected in front of some fairly bright emission and is absorbing or scattering some of that emission.

[6] The Millimeter Wave Observatory was operated by the Electrical Engineering Research Laboratory of the University of Texas at Austin with support from the National Science Foundation and McDonald Observatory.

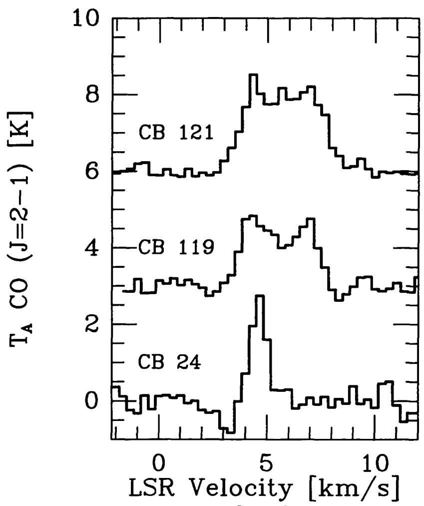

FIG. 4.—Sample ^{12}CO ($J = 2 - 1$) line profiles for three CB clouds. This collection was chosen to illustrate the nature of the most common departures from pure Gaussian line profiles. The bottom spectrum, obtained toward CB 24, is an example of a narrow line (indicated by a "N" in the notes of Table 1). The middle spectrum, from CB 119, exhibits a doubled ("D") line profile. This doubling is likely due to high optical depth and self-absorption of the CO $J = 2 - 1$ line. The top spectrum, from CB 121, shows a wide, or flat-topped ("F"), line profile. Wide lines, especially with square tops, are likely less optically thick versions of the doubled line profile clouds.

III. DISCUSSION

Our analysis of the information contained in Table 1 begins with the most direct, observed characteristics of the *IRAS* and CO data and progresses to the most derivative or speculative findings. Further, the *IRAS* and CO aspects are separately discussed up to the last stage, where correlations between the two wavelengths are sought for this class of clouds.

a) *IRAS Data Characteristics*

Table 1 lists both the integrated fluxes and the estimated uncertainties for each *IRAS* band. From this tabulation, we find that the fraction of clouds in the CB sample which have significantly (> +3 σ) detected fluxes are 98% at 100 μm (243 of 248 clouds), 94% at 60 μm (232 clouds), 91% at 25 μm (226 clouds), and 82% at 12 μm (204 clouds). This extremely high detection rate is a strong testament to the ability of *IRAS* to sense very faint thermal emission from these tiny clouds. The essentially perfect detection rate at 100 μm is exactly that predicted by CB from the log (N)–log (S_{100}) histogram of the PSC detections. One particular advantage of the high co-added data detection rates is that completeness is not a problem; essentially all target objects were seen.

The most basic description of the *IRAS* fluxes contained in Table 1 are displayed in Figure 5 as log (N)–log (S) histograms for the four *IRAS* bands. Both the 12 and 25 μm curves are peaked around 2 Jy, while the 60 and 100 μm curves are shifted to higher flux values. The 60 μm curve is centered near 9 Jy, and the 100 μm curve is centered near 35 Jy. The formal averages and dispersions for the logarithmic distributions are 0.15±0.60, 0.16±0.60, 0.84±0.63, and 1.54±0.55 for the 12, 25, 60, and 100 μm bands. These correspond roughly to 1.4±0.8 Jy, 1.5±0.9 Jy, 7±4 Jy, and 35±19 Jy.

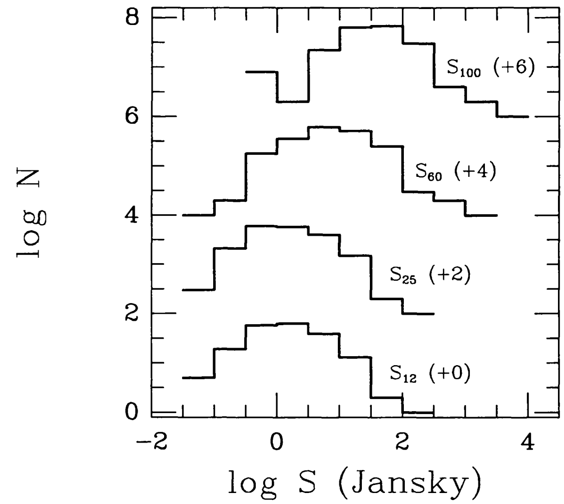

FIG. 5.—log N–log S histograms for co-added *IRAS* matched aperture photometry of CB clouds. Histogram offsets are noted in parentheses.

These mean fluxes were combined into one representative spectral energy distribution for an "average" Bok globule in Figure 6. There log (νF_ν) is plotted versus the *IRAS* band. In the Figure, the cool, long-wavelength dust emission from the bulk of the cloud competes with the very warm, short-wavelength dust emission from small, nonequilibrium dust grains on the edges of the clouds (see Beichman 1988). This spectrum is remarkably similar to the spectrum of diffuse Galactic emission determined by Boulanger and Perault (1988), the spectra of atomic hydrogen clouds determined by Boulanger *et al.* (1985), and the spectra of high-latitude molecular clouds determined by Weiland *et al.* (1986). However, the average Bok globule spectrum is quite different from the spectrum produced by embedded OB stars (Wood and Churchwell 1989).

At this point, it is worth noting that the average spectrum

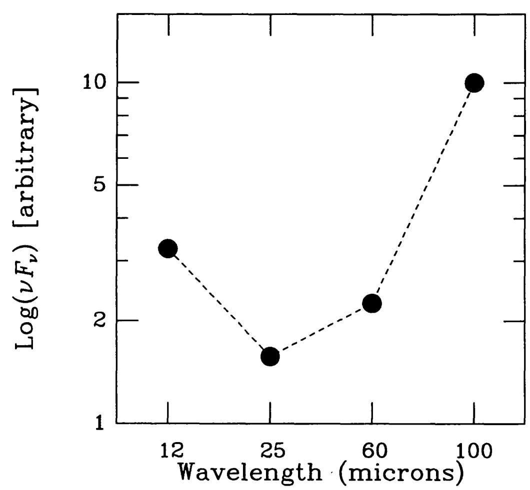

FIG. 6.—Mean far-infrared spectral energy distribution for Bok globules. This spectrum was computed using the average colors of the *IRAS* co-added photometry for the CB clouds. Note the "kink" in the spectrum for the shortest wavelength band.

TABLE 1

CO-ADDED IRAS AND CO SURVEY PROPERTIES

	IRAS					^{12}CO			
No.	S_{12} (Jy)	S_{25} (Jy)	S_{60} (Jy)	S_{100} (Jy)	Area (arcmin^2)	T_R (K)	V_0 (km s^{-1})	ΔV (km s^{-1})	Notes
1	0.57 (0.01)[a]	0.29 (0.02)[a]	3.16 (0.07)[a]	10.55 (0.20)[a]	29	2.77 (0.52)[a]	−3.22	3.84	2
2	0.55 (0.01)	0.62 (0.02)	1.59 (0.06)	7.37 (0.18)	23	3.97 (0.64)	−2.40	1.78	2
3	9.20 (0.05)	9.40 (0.05)	67.62 (0.12)	222.81 (0.52)	199	6.43 (0.42)	38.32	3.08	2
4	1.53 (0.03)	1.55 (0.02)	7.14 (0.07)	29.21 (0.20)	89	6.90 (0.30)	−11.30	0.57	1N
5	−0.37 (0.03)	−0.27 (0.03)	1.27 (0.19)	5.32 (0.55)	36	3.25 (0.48)	4.15	2.04	2D
6	1.36 (0.05)	2.38 (0.02)	9.68 (0.04)	36.16 (0.25)	142	6.18 (0.14)	12.50	0.71	1
7	0.29 (0.03)	0.16 (0.02)	5.67 (0.07)	18.25 (0.25)	37	2.76 (0.27)	0.08	2.34	2F
8	1.31 (0.04)	1.36 (0.02)	3.30 (0.04)	30.58 (0.12)	149	4.56 (0.24)	2.23	2.46	2D
9	0.06 (0.03)	0.29 (0.03)	2.62 (0.12)	10.40 (0.32)	27	2.78 (0.45)	2.71	0.84	2
10	−0.49 (0.02)	−0.09 (0.03)	1.13 (0.09)	14.76 (0.29)	97	4.89 (0.24)	0.54	3.34	2
11	3.11 (0.03)	3.12 (0.02)	15.57 (0.06)	60.54 (0.26)	69	2.03 (0.12)	−1.90	2.13	2
12	0.54 (0.03)	0.62 (0.02)	5.36 (0.05)	29.78 (0.22)	50	6.81 (0.30)	−11.39	2.81	2
13	0.40 (0.02)	0.56 (0.01)	1.44 (0.05)	11.07 (0.28)	29	3.13 (0.41)	35.90	1.28	2
14	0.30 (0.02)	0.60 (0.01)	1.08 (0.05)	10.04 (0.29)	30	4.98 (0.24)	−11.02	2.33	1
15	3.59 (0.05)	2.90 (0.03)	9.97 (0.07)	91.57 (0.47)	192	5.40 (0.83)	0.77	5.99	2
16	1.27 (0.03)	1.12 (0.02)	2.43 (0.04)	18.44 (0.15)	70	5.93 (0.42)	−2.35	0.84	1N
17	0.79 (0.03)	0.93 (0.02)	3.66 (0.04)	16.72 (0.14)	62	5.24 (0.75)	−4.65	0.99	1
18	0.50 (0.02)	0.46 (0.03)	1.11 (0.03)	11.91 (0.16)	33	4.67 (0.34)	−2.87	1.52	1
19	1.17 (0.03)	1.01 (0.06)	1.08 (0.06)	22.30 (0.35)	80	5.70 (0.39)	6.68	1.70	1
20	0.05 (0.01)	0.58 (0.03)	1.55 (0.06)	11.01 (0.25)	41	8.06 (0.55)	5.68	0.84	1
21	0.59 (0.02)	1.48 (0.04)	1.90 (0.05)	7.30 (0.28)	56	2.57 (0.35)	6.78	1.20	3F
22	−0.06 (0.02)	0.02 (0.03)	−0.05 (0.04)	7.14 (0.21)	32	3.05 (0.69)	2.50	2.58	2
23	0.25 (0.01)	0.31 (0.02)	0.59 (0.01)	6.37 (0.17)	27	1.56 (0.27)	5.55	1.51	2D
24	−0.01 (0.03)	−0.20 (0.02)	−0.12 (0.03)	1.80 (0.10)	26	4.87 (0.97)	4.60	0.80	1N
25	0.36 (0.02)	0.15 (0.02)	0.82 (0.02)	8.31 (0.09)	23	4.29 (0.24)	5.20	0.70	1N
26	0.52 (0.04)	0.67 (0.03)	5.92 (0.04)	27.77 (0.14)	52	5.52 (0.58)	5.77	0.90	2
27	0.06 (0.03)	0.28 (0.03)	1.35 (0.06)	23.72 (0.29)	68	5.28 (0.30)	7.14	0.88	1N
28	2.68 (0.04)	3.57 (0.10)	16.77 (0.08)	71.69 (0.52)	116	15.16 (0.55)	8.86	1.02	1
29	6.82 (0.06)	10.38 (0.07)	46.87 (0.11)	157.69 (0.47)	105	17.97 (0.48)	11.20	1.56	1
30	4.97 (0.07)	7.08 (0.16)	24.81 (0.17)	117.69 (0.57)	71	7.58 (0.61)	−0.10	2.07	2
31	3.47 (0.02)	2.31 (0.01)	15.66 (0.55)	67.26 (1.16)	67	5.27 (0.54)	−7.19	1.10	1
32	7.69 (0.01)	9.12 (0.02)	42.36 (0.52)	125.26 (0.50)	95	9.03 (0.42)	−5.07	1.84	1
33	2.85 (0.04)	3.09 (0.06)	10.65 (0.11)	73.91 (0.28)	115	2.49 (0.27)	0.84	2.71	3F
34	1.89 (0.04)	7.20 (0.05)	14.67 (0.10)	44.67 (0.26)	94	2.84 (0.24)	0.73	3.77	3F
35	5.62 (0.07)	6.70 (0.03)	28.17 (0.23)	98.67 (0.56)	72	7.15 (0.48)	9.36	1.13	1N
36	3.71 (0.07)	4.30 (0.04)	10.15 (0.08)	44.07 (0.39)	149	4.00 (0.30)	1.07	1.40	1
37	0.12 (0.02)	0.23 (0.02)	1.09 (0.05)	9.27 (0.23)	37	3.68 (0.27)	1.21	3.55	2F
38	0.01 (0.03)	0.35 (0.04)	0.09 (0.03)	1.53 (0.21)	40	3.40 (0.36)	3.13	0.56	1F
39	4.54 (0.04)	10.30 (0.05)	11.39 (0.05)	28.56 (0.31)	88	4.78 (0.36)	2.35	2.05	2
40	0.50 (0.04)	0.76 (0.05)	3.22 (0.05)	12.02 (0.28)	73	5.43 (0.33)	2.84	1.19	2
41	0.15 (0.04)	0.65 (0.03)	1.54 (0.09)	5.14 (0.26)	44	3.86 (0.21)	2.93	1.16	1
42	−0.05 (0.03)	0.19 (0.02)	0.53 (0.06)	3.97 (0.19)	22	4.48 (0.49)	2.80	2.23	2
43	0.06 (0.03)	0.13 (0.02)	0.74 (0.07)	4.19 (0.21)	28	5.02 (0.41)	3.31	2.30	1
44	0.06 (0.02)	0.70 (0.04)	3.57 (0.17)	23.05 (0.35)	52	4.12 (0.36)	−0.49	1.75	2
45	1.87 (0.08)	3.51 (0.09)	16.31 (0.18)	80.10 (1.00)	110	4.27 (0.30)	0.84	2.16	1
46	0.21 (0.02)	0.62 (0.02)	0.67 (0.02)	5.60 (0.08)	29	2.88 (0.30)	19.46	1.37	1
47	0.05 (0.02)	0.59 (0.02)	0.83 (0.02)	6.61 (0.07)	26	3.25 (0.39)	19.32	1.35	2
48	0.50 (0.02)	1.22 (0.03)	1.79 (0.02)	9.26 (0.09)	43	1.64 (0.21)	18.58	1.56	1
49	0.16 (0.02)	0.31 (0.01)	1.01 (0.03)	8.26 (0.13)	14	4.82 (0.36)	9.59	4.59	3D
50	2.72 (0.04)	3.34 (0.04)	23.19 (0.17)	73.36 (0.53)	86	7.00 (0.64)	0.89	0.65	2
51	1.15 (0.02)	1.52 (0.02)	10.77 (0.14)	26.22 (0.31)	14	0.74 (0.38)	8.07	3.18	3
52	4.90 (0.04)	5.54 (0.04)	20.14 (0.05)	108.49 (0.49)	207	5.06 (0.28)	16.63	4.03	3
53	6.57 (0.04)	2.69 (0.03)	0.67 (0.10)	2.72 (0.53)	55	< 1.0	...	...	...
54	4.47 (0.04)	8.06 (0.02)	69.69 (0.05)	179.71 (0.35)	125	6.26 (0.76)	19.49	4.51	2
55	1.00 (0.02)	0.94 (0.01)	2.13 (0.03)	13.99 (0.22)	47	3.06 (0.33)	19.98	1.60	2
56	1.28 (0.02)	1.72 (0.02)	6.43 (0.05)	19.19 (0.22)	55	3.79 (0.39)	14.51	1.44	1
57	3.55 (0.08)	4.90 (0.05)	17.09 (0.18)	63.92 (0.38)	137	4.44 (0.36)	20.33	2.15	2
58	3.94 (0.06)	4.68 (0.05)	23.54 (0.29)	74.05 (0.92)	87	6.39 (0.33)	15.04	1.67	1
59	2.01 (0.02)	0.87 (0.05)	12.29 (0.08)	70.17 (0.34)	170	3.19 (0.35)	10.59	2.63	2
60	9.55 (0.06)	12.02 (0.07)	54.39 (0.06)	177.76 (0.40)	121	12.88 (0.54)	13.92	1.82	3D
61	0.40 (0.01)	0.38 (0.01)	0.88 (0.01)	5.14 (0.11)	58	< 0.5	...	...	...
62	0.08 (0.01)	0.03 (0.01)	0.08 (0.01)	0.52 (0.01)	18	< 1.0	...	...	...
63	0.61 (0.02)	1.24 (0.07)	4.73 (0.08)	42.66 (0.30)	99	6.24 (0.24)	2.52	0.88	1N
64	0.54 (0.04)	0.58 (0.02)	5.71 (0.08)	32.65 (0.28)	87	2.17 (0.27)	0.70	1.00	1N
65	3.35 (0.11)	2.90 (0.08)	13.15 (0.77)	63.16 (1.98)	24	12.67 (0.67)	2.35	1.34	1N

TABLE 1—*Continued*

No.	IRAS S_{12} (Jy)	S_{25} (Jy)	S_{60} (Jy)	S_{100} (Jy)	^{12}CO Area (arcmin^2)	T_R (K)	V_0 (km s^{-1})	ΔV (km s^{-1})	Notes
66	...[b]	...[b]	23.48 (0.15)	96.97 (0.77)	132	1.96 (0.21)	3.43	0.76	1N
67	9.74 (0.16)	8.81 (0.18)	42.45 (0.30)	264.46 (1.23)	437	9.84 (0.48)	4.80	1.30	1N
68	0.01 (0.04)	1.85 (0.05)	21.29 (0.06)	56.08 (0.68)	66	6.71 (0.52)	5.02	1.38	1
69	12.44 (0.11)	14.00 (0.16)	43.08 (0.23)	193.84 (0.89)	94	6.84 (0.33)	18.52	2.35	2D
70	2.61 (0.11)	3.71 (0.05)	8.36 (0.12)	44.12 (1.10)	77	9.41 (0.54)	2.59	1.05	1N
71	2.98 (0.04)	4.55 (0.05)	15.09 (0.13)	59.70 (0.67)	48	7.75 (0.54)	2.89	1.08	1N
72	−0.15 (0.03)	0.32 (0.03)	2.82 (0.13)	37.34 (0.60)	47	14.22 (0.77)	4.74	1.15	1
73	2.86 (0.07)	3.16 (0.11)	11.12 (0.12)	56.32 (0.75)	71	10.22 (0.44)	13.77	1.59	1
74	0.08 (0.04)	0.82 (0.03)	3.30 (0.10)	36.07 (0.51)	45	11.47 (0.67)	3.84	2.04	1
75	2.64 (0.21)	2.59 (0.22)	10.53 (0.16)	39.41 (0.57)	51	3.03 (0.51)	9.47	2.91	2
76	1.28 (0.09)	1.80 (0.07)	16.74 (0.13)	56.80 (0.62)	133	5.87 (0.39)	1.22	0.92	1N
77	−0.18 (0.02)	0.08 (0.02)	1.42 (0.07)	17.17 (0.09)	69	6.20 (0.50)	−0.32	0.95	1N
78	2.10 (0.05)	5.61 (0.04)	26.08 (0.08)	154.53 (0.76)	190	10.05 (0.61)	4.26	1.06	2F
79	0.54 (0.09)	1.23 (0.05)	9.07 (0.14)	64.54 (1.00)	82	10.17 (0.90)	3.55	2.14	1
80	1.32 (0.06)	1.84 (0.06)	8.23 (0.11)	46.08 (0.86)	100	10.25 (0.39)	2.36	1.39	1
81	1.00 (0.05)	8.40 (0.08)	11.74 (0.22)	99.06 (0.91)	89	11.64 (0.42)	3.52	1.64	3
82	5.72 (0.09)	5.14 (0.05)	5.85 (0.16)	28.60 (0.59)	53	7.83 (0.36)	3.45	0.97	1N
83	0.20 (0.10)	2.39 (0.06)	12.25 (0.18)	45.21 (0.67)	68	7.57 (0.38)	4.98	0.65	1
84	0.23 (0.06)	0.88 (0.03)	3.25 (0.10)	16.15 (0.37)	20	10.89 (0.27)	4.68	0.80	1
85	0.86 (0.08)	1.56 (0.04)	9.79 (0.14)	53.28 (0.51)	40	12.74 (0.54)	5.02	0.76	1N
86	0.78 (0.09)	0.40 (0.05)	6.53 (0.17)	37.91 (0.61)	55	12.63 (0.36)	4.37	1.09	1N
87	3.65 (0.10)	3.53 (0.05)	19.41 (0.18)	86.67 (0.64)	63	15.15 (0.61)	4.66	0.75	1N
88	15.41 (0.24)	14.31 (0.21)	99.97 (0.38)	321.52 (1.93)	239	15.65 (0.48)	3.71	1.17	1N
89	0.80 (0.08)	1.93 (0.06)	14.33 (0.24)	34.75 (0.73)	46	8.32 (0.45)	3.76	1.76	2
90	0.70 (0.20)	0.60 (0.24)	3.96 (0.07)	15.78 (0.38)	30	5.37 (0.30)	10.44	1.64	1
91	0.05 (0.17)	0.33 (0.20)	2.46 (0.06)	9.73 (0.32)	21	2.75 (0.52)	10.49	4.09	3
92	1.99 (0.27)	1.79 (0.33)	7.32 (0.09)	31.92 (0.53)	56	4.54 (0.46)	10.51	2.38	2
93	2.12 (0.21)	1.97 (0.26)	4.13 (0.08)	16.62 (0.42)	35	3.94 (0.42)	10.26	1.43	3
94	0.19 (0.14)	0.28 (0.17)	1.38 (0.05)	3.41 (0.27)	14	4.23 (0.30)	10.64	0.62	1N
95	−0.08 (0.05)	−0.39 (0.05)	0.92 (0.11)	12.90 (0.98)	30	3.58 (0.39)	11.14	0.89	1N
96	0.65 (0.05)	0.09 (0.05)	4.47 (0.12)	29.28 (1.07)	36	3.80 (0.33)	10.80	1.49	2
97	4.71 (0.06)	3.45 (0.06)	14.32 (0.14)	100.02 (1.23)	48	5.30 (0.48)	10.53	1.52	2
98	1.25 (0.03)	0.82 (0.03)	2.47 (0.06)	20.98 (0.58)	10	3.02 (0.36)	10.73	1.50	2
99	1.19 (0.10)	0.80 (0.09)	1.66 (0.07)	14.29 (0.36)	12	3.70 (0.58)	10.63	1.18	2
100	1.31 (0.03)	0.96 (0.02)	8.42 (0.08)	69.43 (0.27)	137	5.99 (0.53)	4.64	1.37	2
101	2.22 (0.02)	1.62 (0.02)	6.71 (0.10)	50.21 (0.29)	94	3.74 (0.48)	6.74	1.23	1
102	12.83 (0.37)	16.85 (0.31)	40.76 (3.62)	185.93 (19.12)	33	6.99 (0.52)	8.27	1.47	1
103	−0.26 (0.02)	0.30 (0.03)	2.53 (0.04)	19.35 (0.17)	50	3.73 (0.33)	5.95	2.58	2
104	8.47 (0.05)	8.72 (0.08)	43.92 (0.17)	242.50 (1.24)	327	2.49 (0.36)	10.59	1.56	1
105	1.10 (0.04)	1.52 (0.02)	7.89 (0.08)	41.57 (0.21)	88	3.21 (0.39)	6.65	2.20	2D
106	1.38 (0.03)	1.45 (0.04)	11.39 (0.12)	61.71 (0.77)	96	5.38 (0.51)	6.22	2.06	2D
107	...[b]	1.04 (0.12)	13.79 (0.79)	30.59 (1.50)	51	5.40 (0.33)	11.56	1.45	1
108	44.22 (0.84)	46.38 (0.78)	403.88 (3.03)	1026.21 (10.89)	78	18.21 (0.80)	5.60	1.87	1
109	1.49 (0.32)	1.29 (0.12)	15.47 (0.25)	50.77 (1.16)	19	2.30 (0.32)	9.61	1.01	3
110	7.80 (0.39)	10.73 (0.33)	20.98 (1.30)	139.44 (6.11)	79	4.25 (0.36)	6.05	1.10	1N
111	12.13 (0.44)	10.30 (0.38)	85.40 (1.46)	198.58 (6.88)	101	4.00 (0.45)	6.97	0.87	1N
112	0.05 (0.05)	0.35 (0.02)	1.64 (0.05)	13.62 (0.31)	31	1.95 (0.33)	13.73	0.80	1N
113	11.65 (0.17)	14.45 (0.24)	52.35 (1.12)	233.86 (3.52)	70	7.61 (0.30)	10.40	5.31	1N
114	8.47 (0.09)	6.62 (0.13)	22.15 (0.62)	64.61 (1.95)	21	6.43 (0.30)	11.93	2.15	1
115	0.75 (0.30)	0.53 (0.15)	8.24 (0.17)	28.19 (0.46)	16	1.58 (0.47)	3.85	1.02	3
116	8.00 (0.11)	5.91 (0.15)	36.88 (0.70)	121.18 (2.20)	27	6.35 (0.36)	11.43	2.45	2
117	−0.27 (0.03)	−0.37 (0.02)	1.49 (0.08)	1.29 (0.26)	27	1.30 (0.36)	1.73	3.94	3
118	21.82 (0.28)	16.12 (0.20)	73.81 (1.35)	342.35 (12.48)	59	4.30 (0.76)	13.08	1.62	2F
119	0.52 (0.03)	0.33 (0.01)	2.79 (0.08)	6.85 (0.25)	25	2.65 (0.24)	5.29	3.57	3D
120	0.23 (0.03)	0.05 (0.02)	2.69 (0.08)	9.50 (0.25)	26	2.82 (0.30)	5.41	3.68	3D
121	3.00 (0.04)	1.39 (0.02)	10.61 (0.12)	21.30 (0.38)	58	3.23 (0.24)	5.70	3.81	3F
122	2.13 (0.03)	1.18 (0.02)	3.65 (0.09)	16.92 (0.28)	32	2.64 (0.21)	6.09	3.74	3D
123	0.49 (0.03)	0.53 (0.02)	0.64 (0.09)	14.72 (0.29)	34	0.70 (0.39)	8.63	2.83	3
124	1.51 (0.02)	1.55 (0.04)	6.23 (0.03)	38.69 (0.21)	138	3.00 (0.22)	20.39	4.21	2
125	195.06 (1.54)	200.24 (1.51)	855.90 (4.81)	2840.80 (25.42)	289	3.24 (0.33)	6.35	2.68	2
126	−0.02 (0.01)	0.22 (0.01)	0.06 (0.03)	8.24 (0.15)	13	2.39 (0.27)	8.34	2.52	2
127	19.55 (0.95)	9.78 (1.84)	144.24 (6.93)	251.08 (32.36)	43	2.82 (0.18)	10.82	2.11	2
128	2.05 (0.02)	1.68 (0.03)	4.50 (0.05)	20.74 (0.26)	42	3.67 (0.42)	8.48	1.47	1
129	0.03 (0.02)	0.25 (0.02)	2.53 (0.04)	25.42 (0.23)	33	3.15 (0.27)	6.46	7.98	3
130	1.14 (0.15)	0.65 (0.06)	6.31 (0.15)	17.13 (0.38)	59	1.41 (0.30)	9.97	1.40	3

TABLE 1—*Continued*

			IRAS				^{12}CO		
No.	S_{12} (Jy)	S_{25} (Jy)	S_{60} (Jy)	S_{100} (Jy)	Area (arcmin^2)	T_R (K)	V_0 (km s^{-1})	ΔV (km s^{-1})	Notes
131	3.38 (0.37)	2.16 (0.32)	21.73 (2.08)	208.51 (12.01)	15	5.39 (0.42)	6.61	1.58	1
132	−0.17 (0.03)	−0.16 (0.04)	0.20 (0.08)	9.41 (0.42)	19	3.23 (0.27)	6.56	2.73	3
133	0.13 (0.01)	0.09 (0.01)	0.09 (0.03)	0.81 (0.20)	7	1.60 (0.33)	4.73	1.18	1N
134	0.33 (0.01)	0.16 (0.01)	0.29 (0.04)	0.86 (0.21)	8	1.68 (0.42)	5.59	0.78	2
135	7.59 (0.13)	4.60 (0.12)	13.82 (0.22)	63.19 (1.57)	55	6.65 (0.49)	13.20	2.74	2
136	0.80 (0.03)	0.34 (0.02)	5.01 (0.09)	19.38 (0.52)	51	3.49 (0.61)	3.69	0.90	3
137	3.59 (0.07)	3.75 (0.09)	47.74 (0.19)	141.63 (0.74)	299	4.48 (0.39)	9.14	1.69	1
138	5.16 (0.26)	4.72 (0.21)	38.54 (1.07)	76.08 (3.12)	23	5.82 (0.58)	6.16	1.64	1N
139	−0.66 (0.19)	−1.13 (0.16)	−4.74 (0.80)	−0.21 (2.33)	13	5.94 (0.36)	5.78	1.59	2
140	8.93 (0.30)	9.08 (0.35)	36.53 (1.39)	209.36 (6.72)	41	5.52 (0.36)	5.87	0.80	1N
141	9.11 (0.46)	8.13 (0.88)	87.68 (7.78)	555.24 (27.43)	11	2.94 (0.48)	5.95	2.62	3
142	3.95 (0.20)	3.47 (0.16)	14.87 (0.67)	69.17 (2.46)	21	9.10 (0.42)	18.63	1.74	1
143	4.26 (0.09)	1.79 (0.07)	16.70 (0.31)	60.59 (0.79)	42	5.88 (0.36)	6.80	0.68	1N
144	0.96 (0.14)	1.70 (0.11)	−11.06 (1.15)	−26.50 (2.69)	33	12.95 (0.69)	15.94	1.50	1
145	50.62 (0.97)	90.16 (1.88)	1225.82 (27.34)	3475.40 (39.65)	78	4.38 (0.36)	4.54	1.46	2
146	21.06 (0.69)	10.18 (1.35)	126.27 (19.55)	374.92 (28.35)	40	4.32 (0.27)	4.28	1.82	2
147	2.20 (0.57)	6.20 (1.11)	26.38 (16.14)	404.82 (23.41)	27	3.13 (0.30)	4.47	2.26	3D
148	11.15 (0.10)	9.23 (0.13)	39.54 (0.16)	159.95 (0.65)	250	5.81 (0.36)	6.54	0.85	1N
149	2.44 (0.30)	1.70 (0.15)	9.06 (0.46)	40.46 (1.19)	32	1.55 (0.25)	−2.00	1.88	2
150	0.05 (0.01)	−0.05 (0.01)	0.40 (0.02)	1.74 (0.08)	15	1.86 (0.27)	4.64	2.23	3
151	1.07 (0.02)	1.41 (0.02)	3.73 (0.03)	18.97 (0.17)	62	3.11 (0.24)	4.79	2.00	2
152	−4.13 (0.50)	6.30 (0.67)	112.57 (4.94)	200.99 (7.07)	65	1.53 (0.15)	4.40	1.14	2
153	0.83 (0.03)	1.15 (0.03)	6.79 (0.12)	24.03 (0.36)	41	2.86 (0.50)	6.15	1.11	2
154	0.78 (0.04)	0.88 (0.02)	2.26 (0.05)	24.39 (0.30)	86	2.26 (0.18)	5.90	2.55	2
155	13.43 (0.36)	10.08 (0.28)	102.92 (2.50)	227.91 (4.90)	66	1.55 (0.36)	6.44	1.81	2
156	0.73 (0.07)	0.35 (0.06)	2.94 (0.26)	12.32 (1.20)	10	3.71 (0.18)	3.55	2.68	2
157	1.01 (0.05)	0.99 (0.03)	11.29 (0.12)	40.58 (0.48)	24	4.63 (0.27)	16.36	1.62	2
158	0.13 (0.04)	0.24 (0.03)	7.89 (0.11)	25.22 (0.44)	21	4.38 (0.76)	15.80	1.66	2
159	0.11 (0.03)	0.26 (0.02)	3.59 (0.08)	10.24 (0.32)	11	4.58 (0.42)	16.21	1.31	1
160	1.67 (0.04)	1.55 (0.02)	2.20 (0.11)	11.18 (0.19)	44	3.64 (0.33)	12.92	0.80	1
161	0.25 (0.03)	0.41 (0.02)	−0.63 (0.09)	2.28 (0.16)	29	2.87 (0.58)	12.56	0.88	1N
162	0.25 (0.03)	0.22 (0.02)	8.28 (0.11)	33.59 (0.81)	33	2.69 (0.33)	16.04	1.44	3D
163	0.00 (0.07)	−0.23 (0.05)	−0.40 (0.38)	2.59 (0.67)	13	4.75 (0.33)	4.22	1.47	1
164	0.56 (0.09)	0.62 (0.06)	7.24 (0.48)	19.23 (0.84)	20	3.37 (0.42)	4.34	1.35	1
165	−0.02 (0.09)	0.11 (0.06)	0.87 (0.49)	24.98 (0.86)	21	3.97 (0.30)	4.96	2.01	1
166	0.43 (0.04)	−0.19 (0.03)	4.90 (0.17)	12.77 (0.65)	43	2.00 (0.31)	15.88	2.10	2
167	−0.10 (0.03)	0.13 (0.02)	1.21 (0.13)	6.62 (0.51)	26	2.48 (0.36)	10.02	0.72	2
168	−0.14 (0.04)	0.50 (0.03)	7.03 (0.17)	37.78 (0.62)	39	3.42 (0.36)	9.71	1.68	2
169	−0.19 (0.03)	0.20 (0.02)	4.68 (0.12)	19.25 (0.46)	21	2.47 (0.58)	9.50	1.15	2F
170	13.95 (0.08)	10.03 (0.03)	14.47 (0.32)	47.95 (0.69)	73	3.86 (0.52)	10.23	0.83	1N
171	2.83 (0.30)	2.43 (0.07)	16.42 (0.16)	78.74 (0.40)	106	3.20 (0.24)	16.74	1.41	3
172	0.92 (0.05)	0.80 (0.02)	3.90 (0.21)	23.58 (0.45)	31	2.86 (0.33)	10.12	0.99	1N
173	0.46 (0.04)	0.72 (0.02)	1.73 (0.16)	8.90 (0.35)	19	6.05 (0.57)	10.67	1.02	1
174	0.80 (0.05)	0.67 (0.02)	3.35 (0.20)	12.56 (0.42)	27	5.43 (0.57)	10.61	1.38	1
175	1.47 (0.05)	1.09 (0.02)	10.02 (0.20)	39.04 (0.44)	29	3.39 (0.66)	10.14	1.62	2D
176	0.08 (0.14)	0.12 (0.03)	3.25 (0.07)	12.26 (0.19)	22	3.73 (0.24)	16.70	1.66	3
177	1.32 (0.04)	1.38 (0.02)	5.30 (0.04)	36.97 (0.20)	87	5.61 (0.42)	16.28	1.64	1
178	3.22 (0.05)	2.26 (0.02)	5.87 (0.05)	55.28 (0.24)	125	4.46 (0.60)	15.33	0.85	1
179	1.27 (0.02)	0.91 (0.04)	11.42 (0.18)	37.72 (0.24)	53	4.82 (0.76)	11.83	1.30	2
180	2.02 (0.03)	2.34 (0.02)	9.81 (0.17)	73.04 (0.81)	83	4.29 (0.39)	11.80	1.56	2
181	0.20 (0.05)	0.68 (0.02)	5.30 (0.12)	27.52 (0.36)	24	4.43 (0.39)	11.31	1.65	1
182	0.39 (0.02)	0.39 (0.02)	2.15 (0.06)	14.50 (0.17)	36	5.41 (0.30)	14.94	1.74	1
183	1.25 (0.03)	0.77 (0.03)	5.69 (0.20)	30.52 (1.12)	39	3.18 (0.86)	6.61	0.53	2
184	2.34 (0.04)	1.33 (0.04)	12.24 (0.26)	60.54 (1.51)	72	1.45 (0.39)	6.27	1.49	2
185	0.03 (0.02)	0.19 (0.01)	0.70 (0.03)	5.73 (0.17)	19	3.16 (0.53)	8.83	0.93	2
186	0.22 (0.03)	0.35 (0.01)	1.01 (0.04)	12.05 (0.22)	30	2.08 (0.25)	9.26	1.21	1
187	0.76 (0.02)	1.20 (0.02)	3.70 (0.08)	47.59 (0.29)	95	2.61 (0.27)	8.99	0.69	1N
188	3.48 (0.14)	3.47 (0.08)	4.14 (0.81)	54.63 (2.83)	29	4.19 (0.42)	7.12	4.40	1
189	−0.82 (0.16)	0.07 (0.09)	−5.99 (0.89)	−7.76 (3.11)	36	4.67 (0.24)	7.63	3.60	2
190	0.70 (0.07)	0.57 (0.05)	5.38 (0.07)	22.41 (0.34)	52	5.67 (0.33)	10.98	1.02	2

TABLE 1—*Continued*

	IRAS					^{12}CO			
No.	S_{12} (Jy)	S_{25} (Jy)	S_{60} (Jy)	S_{100} (Jy)	Area (arcmin^2)	T_R (K)	V_0 (km s^{-1})	ΔV (km s^{-1})	Notes
191	0.08 (0.01)	0.11 (0.01)	0.72 (0.03)	4.96 (0.16)	12	3.09 (0.47)	8.93	0.75	2
192	2.20 (0.08)	1.60 (0.04)	13.10 (0.25)	65.88 (1.22)	22	4.66 (0.37)	6.85	2.53	2D
193	1.19 (0.05)	1.36 (0.04)	9.77 (0.16)	63.58 (0.78)	39	3.92 (0.41)	7.51	2.31	2
194	0.88 (0.84)	0.24 (0.74)	4.19 (0.28)	25.51 (1.27)	40	3.08 (0.24)	3.85	0.82	1
195	0.37 (0.04)	0.30 (0.02)	2.03 (0.04)	14.70 (0.28)	24	5.07 (0.88)	9.62	0.63	2
196	1.20 (0.04)	0.69 (0.02)	6.08 (0.05)	37.85 (0.34)	37	3.88 (0.27)	9.77	0.97	2
197	−0.08 (0.12)	0.21 (0.05)	2.59 (0.25)	8.11 (0.92)	19	4.23 (0.30)	24.49	1.24	1
198	1.26 (0.04)	0.30 (0.02)	3.87 (0.05)	20.31 (0.33)	34	4.12 (0.24)	9.81	0.60	1N
199	2.97 (0.07)	1.75 (0.04)	15.47 (0.12)	75.66 (0.31)	115	4.17 (0.27)	8.39	1.29	1
200	0.41 (0.02)	0.33 (0.02)	3.25 (0.04)	18.99 (0.17)	30	2.42 (0.33)	9.61	1.03	3
201	0.41 (0.03)	0.56 (0.03)	4.69 (0.06)	16.18 (0.25)	65	3.30 (0.35)	9.71	0.92	2
202	0.64 (0.06)	0.99 (0.04)	5.34 (0.11)	37.90 (0.61)	38	3.82 (0.70)	18.12	0.76	2
203	6.27 (0.10)	5.04 (0.07)	27.59 (0.17)	146.71 (0.99)	102	2.72 (0.24)	15.82	1.26	1
204	0.01 (0.02)	0.19 (0.01)	0.33 (0.04)	6.69 (0.16)	22	5.83 (0.30)	7.62	1.02	1N
205	3.84 (0.05)	9.22 (0.05)	54.51 (0.40)	154.43 (0.98)	67	5.48 (0.58)	15.77	3.38	1
206	10.56 (0.09)	9.54 (0.06)	35.01 (0.25)	220.44 (0.90)	206	4.50 (0.36)	15.27	1.85	1
207	1.34 (0.05)	0.54 (0.02)	3.18 (0.09)	16.20 (0.43)	42	2.94 (0.39)	7.56	1.26	2F
208	0.41 (0.04)	0.84 (0.03)	2.94 (0.11)	21.74 (0.39)	38	5.17 (0.36)	15.29	1.35	1
209	1.55 (0.03)	1.07 (0.01)	3.53 (0.06)	15.39 (0.26)	30	4.10 (0.39)	16.07	1.10	1
210	0.34 (0.02)	0.26 (0.02)	1.34 (0.08)	9.05 (0.35)	22	3.33 (0.36)	9.67	2.11	1
211	1.03 (0.28)	1.12 (0.14)	2.88 (0.07)	18.34 (0.60)	36	2.17 (0.15)	7.06	2.79	1
212	0.77 (0.03)	0.71 (0.01)	3.98 (0.04)	16.68 (0.22)	48	5.86 (0.64)	16.64	1.48	1
213	0.82 (0.31)	0.87 (0.15)	5.57 (0.08)	36.78 (0.67)	45	1.79 (0.24)	7.60	1.16	1
214	0.51 (0.05)	0.50 (0.04)	3.76 (0.11)	23.65 (0.57)	21	2.18 (0.33)	9.94	1.30	1
215	0.28 (0.04)	0.21 (0.03)	2.01 (0.10)	16.69 (0.52)	18	3.06 (0.24)	9.11	2.81	2
216	7.18 (0.06)	11.78 (0.05)	34.97 (0.20)	150.52 (0.86)	169	4.03 (0.33)	12.59	2.64	2D
217	13.56 (0.22)	13.05 (0.10)	89.94 (0.70)	256.28 (1.46)	49	4.77 (0.20)	−0.47	2.28	1
218	0.41 (0.01)	0.71 (0.02)	1.92 (0.02)	14.49 (0.13)	32	5.21 (0.51)	9.84	0.97	1
219	0.10 (0.01)	0.12 (0.01)	0.67 (0.02)	4.28 (0.12)	40	4.42 (0.47)	−1.83	0.51	1
220	0.50 (0.01)	0.40 (0.02)	0.80 (0.02)	7.40 (0.07)	82	4.49 (0.27)	3.19	0.80	1
221	0.55 (0.01)	0.45 (0.01)	1.98 (0.03)	9.37 (0.26)	31	3.15 (0.55)	13.81	1.89	1
222	0.47 (0.01)	0.21 (0.01)	0.78 (0.04)	7.34 (0.16)	44	1.95 (0.30)	0.05	1.37	3
223	0.14 (0.01)	0.08 (0.01)	0.02 (0.03)	0.91 (0.12)	22	3.24 (0.39)	−2.63	0.79	1
224	1.93 (0.01)	2.44 (0.02)	10.43 (0.06)	50.66 (0.23)	92	3.38 (0.48)	−2.73	2.73	3
225	0.25 (0.03)	0.31 (0.01)	1.65 (0.05)	36.09 (0.36)	77	4.10 (0.37)	−2.46	2.87	2D
226	0.15 (0.02)	0.05 (0.03)	0.10 (0.05)	14.29 (0.51)	44	3.87 (0.39)	−1.87	1.10	1N
227	0.17 (0.02)	0.07 (0.02)	0.20 (0.05)	8.65 (0.43)	31	2.58 (0.27)	−1.86	1.64	3D
228	0.54 (0.03)	0.21 (0.03)	1.37 (0.09)	8.45 (0.28)	43	2.99 (0.69)	−1.65	0.79	2
229	1.31 (0.01)	1.21 (0.02)	5.05 (0.03)	33.62 (0.20)	94	3.82 (0.47)	3.40	0.78	2
230	0.80 (0.02)	1.07 (0.01)	15.55 (0.07)	64.66 (0.52)	98	3.38 (0.21)	2.86	0.95	1N
231	1.33 (0.02)	1.03 (0.02)	2.94 (0.09)	24.62 (0.39)	55	4.57 (0.24)	6.50	1.69	1
232	1.59 (0.15)	5.26 (0.04)	11.76 (0.11)	56.77 (0.30)	111	4.88 (0.27)	12.59	2.22	1
233	0.51 (0.15)	1.37 (0.07)	20.79 (0.17)	38.42 (1.10)	77	4.08 (0.39)	−0.93	1.05	1
234	−0.17 (0.04)	0.18 (0.02)	4.37 (0.05)	64.50 (0.42)	136	4.35 (0.41)	−4.96	1.75	3F
235	0.60 (0.04)	0.32 (0.04)	0.94 (0.12)	1.13 (0.82)	28	3.48 (0.30)	−1.81	2.19	1
236	0.32 (0.03)	0.41 (0.06)	0.13 (0.23)	0.91 (0.66)	21	1.81 (0.15)	−2.93	1.69	1
237	0.94 (0.04)	0.43 (0.09)	9.44 (0.49)	14.72 (0.56)	62	4.48 (0.48)	−2.93	2.34	2D
238	0.17 (0.01)	0.13 (0.01)	1.50 (0.01)	17.69 (0.11)	48	6.33 (0.41)	0.23	1.60	1
239	0.45 (0.02)	0.37 (0.01)	0.98 (0.03)	2.61 (0.07)	75	. . .[c]	. . .[c]	. . .[c]	. . .[c]
240	4.62 (0.01)	5.77 (0.01)	37.97 (0.47)	102.86 (1.39)	46	4.72 (0.65)	−3.61	0.87	1
241	0.71 (0.04)	0.19 (0.02)	5.21 (0.12)	27.31 (0.34)	55	5.23 (0.36)	−7.58	1.66	2
242	2.92 (0.06)	6.47 (0.18)	17.86 (0.38)	37.23 (1.13)	37	5.76 (0.36)	−10.90	2.22	2
243	4.97 (0.03)	6.43 (0.10)	31.94 (0.40)	90.45 (0.41)	120	7.19 (0.42)	−11.07	1.56	1
244	1.60 (0.05)	2.72 (0.06)	17.68 (0.04)	112.31 (0.69)	223	6.12 (0.54)	3.93	2.48	2D
245	1.06 (0.02)	1.00 (0.03)	4.74 (0.11)	29.45 (0.65)	16	4.03 (0.30)	−0.76	1.54	3
246	−0.91 (0.03)	−0.11 (0.04)	−0.29 (0.14)	14.00 (0.80)	24	4.82 (0.24)	−0.46	1.62	1
247	2.45 (0.08)	2.88 (0.05)	11.48 (0.29)	58.27 (0.62)	95	4.87 (0.33)	−3.73	1.13	1
248	0.79 (0.02)	0.76 (0.02)	2.10 (0.03)	16.71 (0.09)	103	7.42 (0.36)	−9.53	0.84	1

[a] Uncertainties noted in parenthesis are 1 σ values.
[b] Not photometered.
[c] Not observed.

shown in Figure 6 cannot be represented by any single-temperature blackbody (even modified by normal wavelength-dependent emissivity terms). Instead, the far-infrared emission from these globules arises from many different dust grain components, each at a somewhat different physical temperature. This is to be expected, since the shape of the interstellar extinction curve seems to require a range of dust grain sizes (Mathis *et al.* 1977) and corresponding temperatures. Additionally, the shorter wavelength *IRAS* emission likely originates from transiently heated, nonequilibrium small dust grains or PAHs (see Puget and Léger 1989). These factors compromise our desire to extract detailed physical information from the measured *IRAS* fluxes, as will be noted in later sections.

Histograms of the logarithms of neighboring *IRAS* band flux ratios ("colors") were constructed for all *IRAS* band pairs. The mean color and dispersion found were 0.70 and 0.22, respectively, for the 100/60 μm color [= log (S_{100}/S_{60})]. Similarly, the mean colors and dispersions were 0.68 and 0.34 for 60/25 μm and 0.01 and 0.30 for 25/12 μm. The nonneighboring band colors and dispersions were as follows: 100/25 μm, 1.38±0.34; 100/12 μm, 1.39±0.37; 60/12 μm, 0.69±0.37. These colors are very typical of molecular clouds in the Galactic plane. Hence, selection of a sample of Bok globules in any two-color *IRAS* diagram will be strongly contaminated by other Galactic molecular clouds.

Correlations of the dust colors were sought by comparing the *IRAS* colors of the globules between different pairs of bands. In Figure 7, the 12 to 25 μm color (log of the flux ratio) for each detected globule in Table 1 is plotted versus the corresponding 25 to 60 μm color. There is a weak anticorrelation, with slope −0.28±0.06 (linear correlation coefficient $R = -0.3$). The sense of the slope is that a cooler, less positive 12/25 μm flux ratio is correlated with a warmer 25/60 μm ratio. This can occur if the 25 μm flux value changes independently of the 12 and 60 μm, though the slope expected for this explanation ought to be roughly −1. The effect seen could also represent a trade-off between 25 μm emission generated by nonequilibrium grains (hot) and 25 μm emission generated by equilibrium grains in high optical depth clouds (cool) (e.g., Heyer *et al.* 1989). Depending on the cloud conditions, one case or the other might prevail, leading to the weak anticorrelation in the sample.

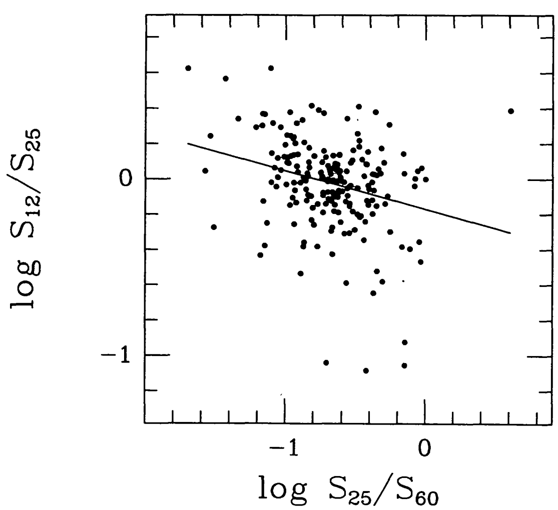

FIG. 7.—Color-color plot for CB clouds in the 12/25 μm and 25/60 μm two-color plane. The colors are represented as the log of the observed co-added flux ratios for each pair of *IRAS* bands. The distribution of CB clouds was fit linearly to yield the line shown. The slope of the line is −0.28±0.06 with linear correlation coefficient $R = -0.3$. The sense of the slope is such that a warmer 12/25 μm color is associated with a cooler 25/60 μm color. Equivalently, a change in the 25 μm emission unrelated to the 12 and 60 μm emission could produce both effects, though the slope of the line should be much steeper (equal to −1).

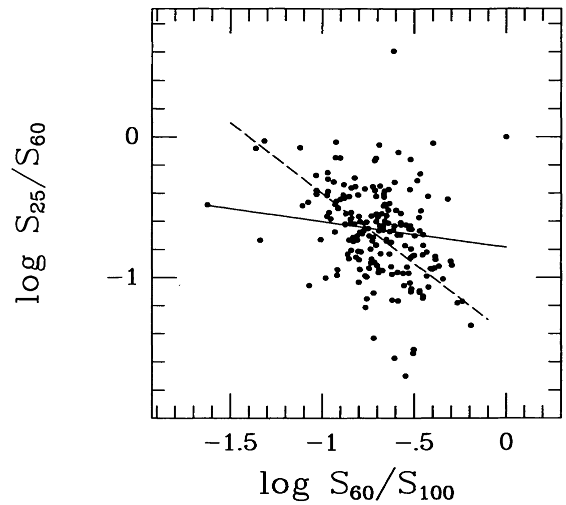

FIG. 8.—Color-color plot for CB clouds in the 25/60 μm and 60/100 μm two-color plane. The colors are represented as the log of the observed co-added flux ratios for each pair of *IRAS* bands. The best-fit line has a slope of −0.46±0.10 ($R = -0.3$; *solid line*), though the distribution of points is not strongly dissimilar to the expected slope of −1 (*dashed line*) for changes in the 60 μm emission level.

Figure 8 presents the 25 to 60 μm color versus the 60 to 100 μm color, similarly showing a weak anticorrelation, with a slope of −0.46±0.10 (and $R = -0.3$). In Figure 8, the best-fit line is shown as a solid line, but another line, with slope −1, is indicated by the dashed line. The data seem to show a similar correspondence with this latter line. This correlation could arise if the 60 μm flux is fairly independent of the 25 and 100 μm fluxes. Such a situation might occur if quite different dust grain sizes and temperatures predominate at the different *IRAS* bands. In that case, the anticorrelation merely underscores the disconnection of the dust properties between the different bands.

Finally, Figure 9, which compares the *independent* 12 to 25 μm and 60 to 100 μm colors, shows a lack of a correlation. We conclude that across the largest wavelength range, there is virtually no correlation of the dust temperatures for these clouds. Cold 60/100 μm ratios are equally well-correlated with hot, cold, and temperate 12/25 μm ratios.

The *IRAS* color-apparent magnitude diagram can be seen in Figure 10, where the 60 to 100 μm color is displayed versus the log of the 100 μm flux. In the plot, the data have been binned and averaged in log flux bins, each 0.2 dex wide. Bins with only one cloud have no error bars. Bins with more than one cloud have error bars reflecting both the dispersion in the bin and the error in the mean (distant and nearby error bars, respectively). Excluding the first three and last three bins,

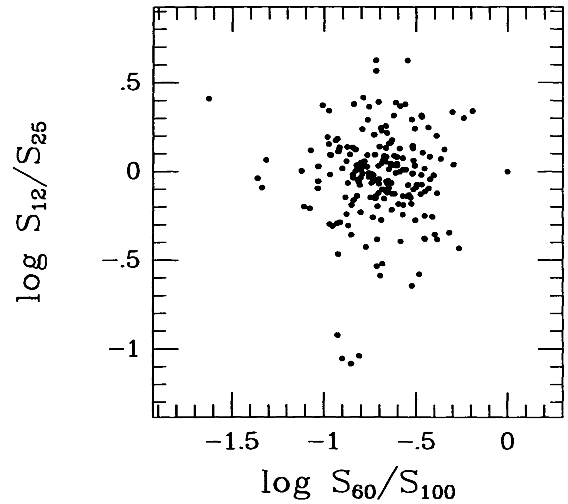

FIG. 9.—Color-color plot for CB clouds in the 12/25 μm and 60/100 μm two-color plane. This plane is insensitive to correlations induced by single-band emission variations or photometric errors. The best-fit line, with slope -0.054 ± 0.095, is hardly significant, indicating relatively little coupling between the FIR emission produced by the bulk of each cloud, as traced by the 60/100 μm color, and the FIR emission produced by the small grains or the cloud surfaces, as traced by the 12/25 μm color.

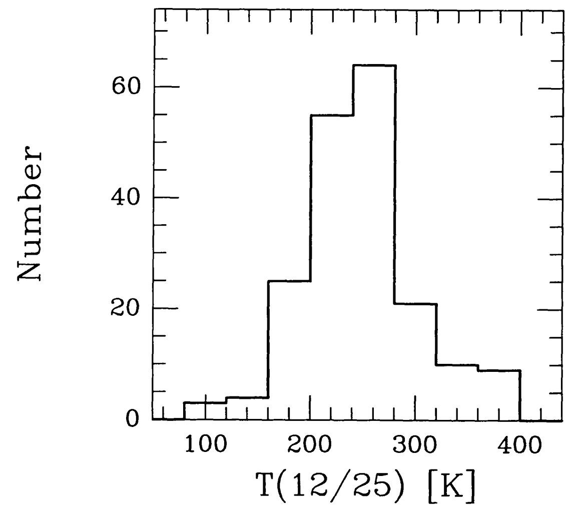

FIG. 11.—Histogram of derived blackbody temperatures for the clouds in Table 1 derived from their 12 and 25 μm flux ratios assuming a λ^{-1} emissivity. The mean temperature is 254 K, with a dispersion of 70 K. There are no temperatures below 80 K. Three clouds (not plotted) have detected temperatures above 440 K.

there is a good correlation, shown by the best-fit line, with slope 0.12 ± 0.02 and a very high correlation coefficient (0.92). The sense of the correlation is that brighter clouds are also warmer. The slope seen probably indicates that the data have a mixture of temperature and distance effects and possibly grain composition effects, as well. Presumably, one could insist that the slope *be* identical to that produced by a blackbody plus wavelength-dependent emissivity and derive some estimate for cloud distances. However, zero-point distance calibration is needed. Additionally, cloud optical depth differences at these wavelengths will strongly affect both the apparent color of a cloud and its 100 μm flux. If all the clouds were at the same distance and had identical dust properties, then a warmer temperature should produce a 100 μm flux increase with a characteristic slope of 0.51 for a dust emissivity law dependent on wavelength as λ^{-1} and 0.52 for a λ^{-2} emissivity, both slopes being much steeper than that found above.

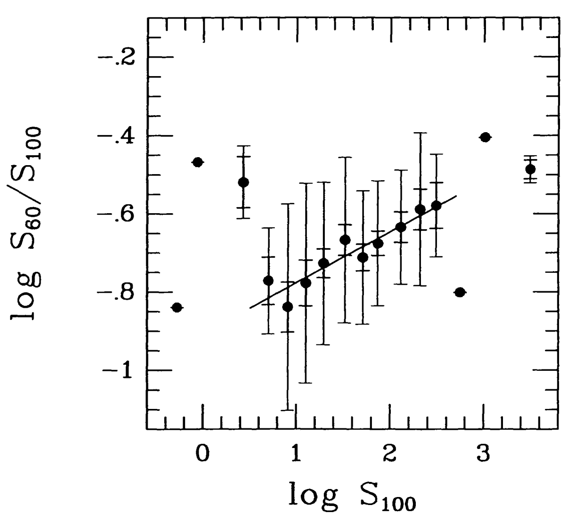

FIG. 10.—Color-apparent magnitude diagram for CB clouds. The color is the log of the 60 to 100 μm flux ratio and the apparent magnitude is represented by the log of the 100 μm flux. The data have been binned into 0.2 dex flux bins. For bins with only one data point, no error bars are shown. For the remainder of the bins, the error bars reflect both the dispersion of the values in each bin and the mean error of the average color for the bin (hence the two sets of errors for each point). Excluding the first and last three data bins, the best-fit line has a slope of 0.12 ± 0.02 and a high correlation coefficient (0.92). The sense of the line is that the brighter globules are warmer. If this flux increase were due entirely to warmer blackbody emission, the expected slope of the correlation would be 0.51.

The next level of analysis consisted of analyzing the *IRAS* fluxes using a single-temperature model. Since the average spectrum (Fig. 6) is definitely not a blackbody, one might expect to see different temperatures characterizing the different pairs of bands. In Figures 11, 12, and 13 we show the temperature histograms for the clouds in Table 1, computed from the 12 to 25 μm, 25 to 60 μm, and 60 to 100 μm flux ratios, assuming the dust has a λ^{-1} emissivity, and using the look-up table scheme of the Appendix. These cloud temperatures are also listed in Table 2. The histograms are fairly strongly peaked at 250 K for the 12/25 μm ratio, 65 K for the 25/60 μm ratio, and 26 K for the 60/100 μm ratio. The computed means and dispersion, for the clouds with good detections ($>3\ \sigma$), are 254 ± 72 K, 71 ± 16 K, and 26 ± 5 K, respectively. Note that none of the 12/25 μm ratios imply temperatures below 100 K, and there are few above 420 K. In virtually no cases are we detecting the photospheres of normal stars projected in front of the clouds—we are detecting the short-wavelength emission from the clouds themselves. Similarly, the 60/100 μm ratios do not fall below 12 K, nor above 42 K. As will be shown below, if the bulk of the dust mass emitted at these wavelengths, these relatively warm 60/100 μm temperatures would be surprising. Changing the emissivity law from λ^{-1} to λ^{-2} does not have a strong effect on these temperatures. The corre-

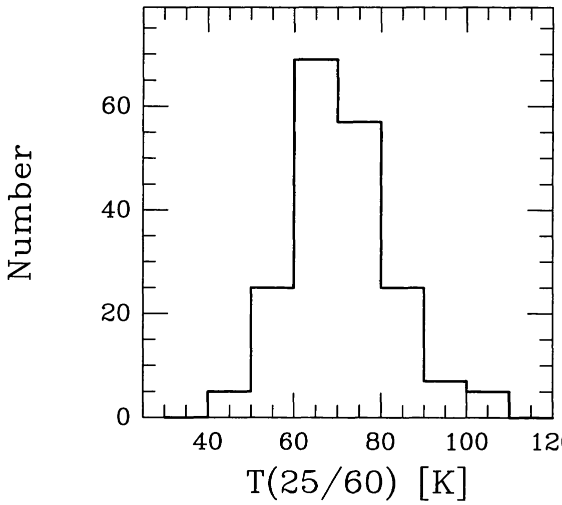

FIG. 12.—Histogram of derived blackbody temperatures for the 25 and 60 μm flux ratios assuming a λ^{-1} emissivity. The mean temperature is 71 K, with a dispersion of 16 K. There are no temperatures below 40 K. One cloud (not plotted) has temperature above 120 K.

sponding mean temperature change to 199±58, 60±11, and 22±4 for the 12/25 μm, 25/60 μm, and 60/100 μm flux ratios.

These derived temperatures should be viewed with a great deal of caution. We have already noted that single-temperature models are incapable of describing the spectral energy distribution of the globules. Further, for the optically thin emission detected from these clouds by *IRAS*, the exponential nature of the flux dependence on temperature (Fig. 10) leads to a bias toward higher derived temperatures than are physically present along the line of sight. Hence, *all* of the temperatures derived are weighted toward the warmer parts of the clouds and not the mass-averaged bulks of the clouds (see Snell, Heyer, and Schloerb 1989). This error is compounded when these derived temperatures are used to derive opacities, as below. Note, then, that all temperatures are upper limits, and all opacities are lower limits.

Once a single temperature has been determined for a pair of *IRAS* bands, the flux density in either band can be used to derive an estimate of the optical depth of the cloud at that wavelength (with the caveat that the mean optical depth computed will be different than that derived from measurements which highly resolve the spatial variations of the cloud emission). Figure 14 indicates the log (N)–log (τ) histogram for the CB clouds at a wavelength of 100 μm, using the 60/100 μm temperature and λ^{-1} emissivity. These derived 100 μm opacities are also listed in Table 2. The mean of the log distribution is −3.60±0.72, and shifts only slightly, to −3.25±0.72, for a λ^{-2} emissivity. The clouds are very optically thin at this wavelength. However, for a minimum optical extinction at V band of 3–5 magnitudes, one would expect to see 100 μm optical depths of 2×10^{-3}–3×10^{-3}, using the dust grain properties of Hildebrand (1983). The ratio of expected-to-observed optical depths is around 9 and indicates the relative fraction of dust in the clouds which is not strongly active at 60 and 100 μm (≈89%).

The nature of this discrepancy can be partially understood by plotting the derived blackbody temperature against the derived far-infrared dust opacity, as has been done in Figure 15. There log (τ_{100}) is plotted versus the log of the derived 60/100 μm temperature. There is a very strong anticorrelation, with a slope of −5.44±0.33, in the sense that as the derived temperature increases, the optical depth decreases. This relation can be rewritten in more convenient form as

$$\tau_{100} = 2.1 \times 10^{-4}\left(\frac{T}{26}\right)^{-5.44} . \quad (1)$$

In Figure 16, this anticorrelation can be seen to primarily arise as a consequence of the single-temperature blackbody

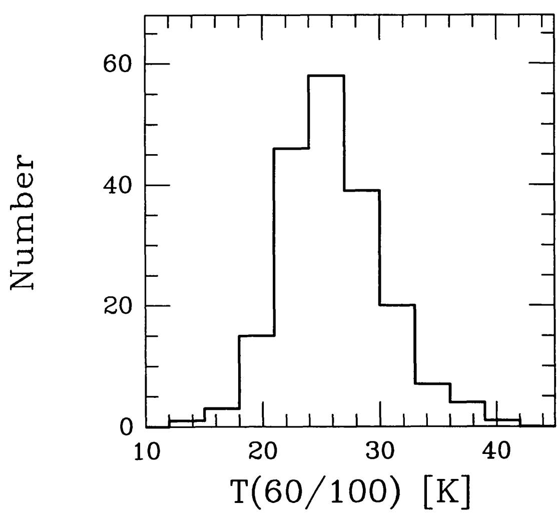

FIG. 13.—Histogram of derived blackbody temperatures for the 60 and 100 μm flux ratios assuming a λ^{-1} emissivity. The mean temperature is 26 K, with a dispersion of 5 K. There are no temperatures below 12 K. One cloud (not plotted) has a temperature above 42 K.

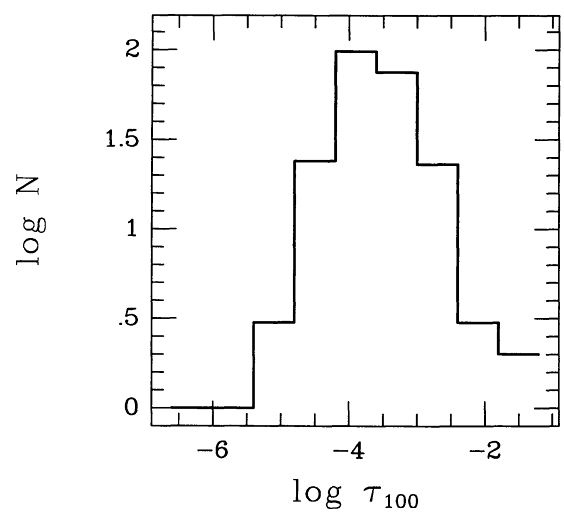

FIG. 14.—Distribution of derived mean dust opacities using the single-temperature blackbody model with λ^{-1} emissivity. The plot displays the distribution of log (N) vs. log ($\tau_{100\ \mu m}$). The mean opacity is −3.60, with a dispersion of 0.72 dex. There are almost no opacities smaller than 1.5×10^{-5} or larger than 0.006. For a λ^{-2} emissivity, the mean of the distribution shifts to −3.25.

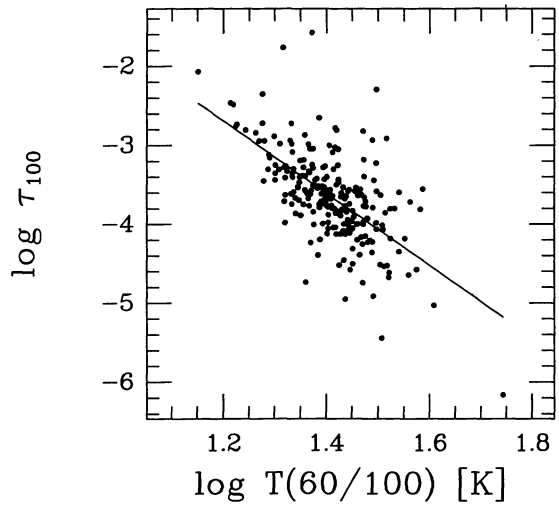

FIG. 15.—Correlation of derived 100 μm dust opacity and dust temperature, measured between 60 and 100 μm, both expressed in logarithmic form. The very strong correlation seen, with slope of -5.44 ± 0.33, implies that dust with higher opacity is characteristically cooler, while thinner dust is hotter.

model. If the 60 μm flux is doubled, the inferred blackbody temperature will increase, and the inferred opacity will decrease. The direction of motion for the clouds in Figure 15 is indicated by the arrows in Figure 16. Most of the motion is along the direction of the anticorrelation seen, indicating that an inappropriate temperature (or temperature distribution) has likely been assigned for several of the clouds, leading to extreme values of both temperature and opacity. However, there is a nonnegligible fraction of the movement of the points in Figure 16 which is not along the anticorrelation line of Figure 15. This indicates that some of the spread in the objects in Figure 15 is probably intrinsic, although most is likely due to the assumption of a single blackbody temperature.

Since the short-wavelength emission seen in the *IRAS* bands has been shown to arise in the outer layers of other larger molecular clouds (e.g., B5; Beichman *et al.* 1988), we wondered if the *IRAS* traced opacities of our clouds might depend on the ratio of surface area to volume. In particular, if the 12 and some of the 25 μm emission arise in a fixed thickness of "skin" around a cloud, then the 12 to 25 μm color and opacity might be expected to depend on the total optical depth through a cloud, in the sense that as the optical depth increased, the average "skin" temperature might decrease as more 25 μm emission was generated by the cloud bulk and the ratio of 12 μm opacity to 100 μm opacity might drop. In Figure 17, we show how the ratio of opacity computed at 12 μm, from the 12 and 25 μm fluxes, to opacity at 100 μm depends on 100 μm opacity. Opacities at 100 μm in excess of 0.01 (two clouds) were believed to be spurious and were not included in this analysis. The best-fit line in the log-log plot has slope -0.52 ± 0.04. This slope is intermediate between the slope of -1 expected for a constant-thickness 12 μm emissive shell for each cloud, and the slope of 0 expected for complete mixing of the small dust grains throughout the volume of each cloud. The intermediate slope correlation seems to imply that the small, hot grains must be at least partially distributed throughout the entire volume of these clouds. This conclusion is in contrast to the situation in B5 (Beichman *et al.* 1988), where the hot grains appear predominantly on the cloud edges. However, our test is not as decisive as a test for the spatial variation of the 12/25 μm ratio across the cloud surface areas. This latter test is beyond the scope of this paper, but will be attempted for the brighter CB clouds in future work.

If the small, nonequilibrium grains are distributed through the volumes of these clouds, how does their heat source, the

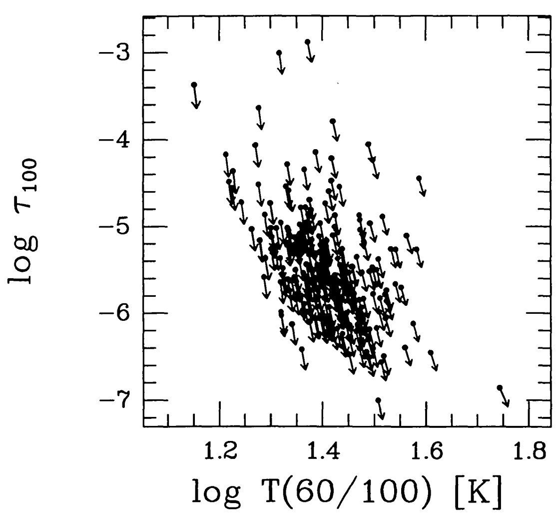

FIG. 16.—Same as Fig. 15, but with arrows indicating the direction of motion of each data point for a change in the 60 μm flux. For the warmer clouds, the predominant direction of motion is along the correlation direction, indicating that the spread along this direction is an artifact of the single-temperature modeling and is not due to a real astrophysical effect. For the cooler clouds, however, the direction of motion is predominantly vertical, indicating that the spread in temperature will not be reduced by a more elaborate model.

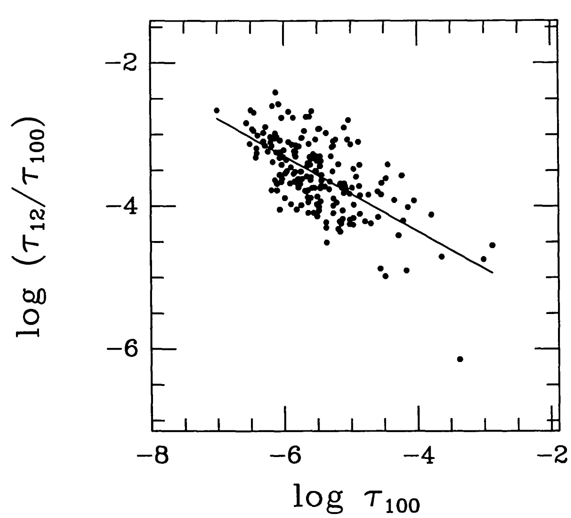

FIG. 17.—Plot of the ratio of 12 μm opacity to 100 μm opacity *versus* 100 μm opacity. The 12 μm opacities were computed from the 12 and 25 μm fluxes using a single-temperature model with λ^{-1} emissivity. The slope of this fitted line is -0.52 ± 0.04, midway between the slopes expected for small grains fully mixed throughout the cloud volumes (slope of 0) and for a fixed small grain layer thickness for each cloud (slope of -1).

TABLE 2

DUST PROPERTIES FROM THE SINGLE-TEMPERATURE BLACKBODY MODEL WITH λ^{-1} EMISSIVITY

Number	T(12/25) [K]	T(25/60) [K]	T(60/100) [K]	$-\log \tau_{100}$	Cloud group
1	336	58	29.5	4.253	C
2	233	81	26.2	4.040	A
3	243	64	29.6	3.771	C
4	244	70	27.4	4.129	A
5	...[b]	< 57[a]	27.2	4.460	A
6	199	72	28.3	4.312	A
7	316	48	29.9	4.151	A
8	242	82	20.9	3.627	A
9	< 144	61	27.7	4.082	A
10	...	< 56	19.0	3.449	C
11	245	69	27.9	3.744	A
12	232	61	24.6	3.614	C
13	216	80	22.2	3.532	A
14	191	89	20.9	3.410	A
15	269	75	21.0	3.266	C
16	259	84	22.3	3.695	A
17	231	72	26.3	4.125	A
18	252	82	20.0	3.251	A
19	261	104	16.8	2.756	A
20	117	80	22.7	3.750	A
21	178	98	28.0	4.581	A
22	...	...	< 12.8	> 1.711	C
23	225	88	20.0	3.439	A
24	...	...	< 16.2	> 3.226	A
25	372	68	20.4	3.303	A
26	223	61	26.1	3.802	A
27	< 146	69	17.5	2.810	A
28	220	70	26.9	3.816	B
29	209	70	29.4	3.629	B
30	215	75	26.0	3.301	A
31	293	64	26.9	3.604	A
32	230	70	30.9	3.788	B
33	238	75	22.9	3.387	C
34	157	86	30.6	4.205	C
35	229	71	29.0	3.635	A
36	232	82	26.8	4.124	A
37	192	70	21.5	3.614	C
38	< 97	> 192	< 17.8	> 3.826	A
39	183	103	33.0	4.527	A
40	208	71	28.3	4.505	A
41	150	82	29.5	4.743	A
42	< 182	78	22.4	3.888	A
43	< 185	67	24.4	4.195	A
44	119	68	23.4	3.616	A
45	195	70	25.7	3.630	A
46	169	103	21.6	3.741	A
47	118	95	21.9	3.665	A
48	179	94	25.2	4.121	A
49	193	76	21.7	3.295	C
50	227	64	30.1	3.923	A
51	220	64	33.4	3.803	C
52	234	74	24.9	3.693	C
53	380	199	27.4	4.950	...[c]
54	198	61	32.6	3.856	C
55	251	83	23.3	3.768	A
56	219	73	30.8	4.358	A
57	217	75	28.3	4.049	A
58	230	69	30.2	3.926	A
59	368	56	24.4	3.746	C
60	225	70	29.7	3.659	B
61	252	83	24.2	4.396	...[c]
62	376	83	22.9	4.739	...[c]
63	190	73	21.1	3.330	A
64	239	60	24.4	3.786	A
65	261	70	25.9	3.088	B
66	...[d]	...[d]	27.3	3.768	A
67	256	69	23.7	3.505	B
68	< 65	58	32.4	4.069	A
69	234	77	26.5	3.251	A
70	215	83	25.0	3.671	B
71	209	76	27.7	3.579	A
72	< 163	61	18.9	2.720	B
73	236	74	25.4	3.566	B
74	< 123	72	19.9	2.886	B
75	248	72	28.3	3.830	C
76	216	60	29.3	4.167	A
77	< 226	54	19.4	3.305	A
78	174	70	24.1	3.421	B
79	183	63	22.7	3.279	B
80	216	70	24.5	3.714	B
81	127	95	21.5	2.979	B
82	257	102	25.7	3.766	A
83	< 117	68	28.4	3.908	A

TABLE 2—*Continued*

Number	T(12/25) [K]	T(25/60) [K]	T(60/100) [K]	$-\log \tau_{100}$	Cloud group
84	156	74	25.6	3.584	B
85	197	65	24.8	3.282	B
86	335	54	24.3	3.516	B
87	249	67	26.5	3.431	B
88	253	64	29.9	3.709	B
89	180	63	33.5	4.183	A
90	> 262	< 65	27.6	3.943	A
91	...	< 63	27.7	4.009	C
92	257	72	26.8	3.837	A
93	253	85	27.5	3.983	A
94	...	< 69	33.2	4.675	A
95	...	< 64	18.6	2.944	A
96	> 1370	< 45	23.3	3.343	A
97	280	72	22.8	2.871	A
98	295	77	21.5	2.723	A
99	292	85	21.4	2.942	A
100	280	61	21.7	3.337	A
101	281	72	22.3	3.401	A
102	221	82	26.3	2.804	A
103	< 148	61	22.2	3.523	C
104	243	69	24.7	3.520	A
105	217	68	25.0	3.759	A
106	241	62	24.8	3.602	A
107	...[d]	56	34.7	4.353	A
108	241	61	32.8	2.911	B
109	261	57	29.7	3.395	A
110	217	87	23.2	2.987	A
111	263	62	34.0	3.801	A
112	< 131	70	21.6	3.401	A
113	226	74	26.5	3.048	C
114	272	75	31.1	3.442	A
115	< 287	55	29.2	3.557	A
116	279	65	29.7	3.180	A
117	...	< 49	55.4	6.163	C
118	279	70	26.2	2.778	A
119	302	61	33.3	4.615	C
120	575	45	28.9	4.201	C
121	354	63	36.3	4.643	C
122	321	77	26.2	3.822	C
123	237	100	16.3	2.465	C
124	243	72	23.7	3.844	C
125	243	71	29.6	2.821	C
126	< 132	> 177	< 11.4	> 0.647	C
127	339	55	38.6	3.555	A
128	266	80	26.2	3.858	A
129	< 129	59	20.4	2.981	C
130	318	60	32.0	4.516	A
131	299	59	20.7	1.768	A
132	...	...	< 13.9	> 1.731	C
133	284	> 107	< 21.0	> 3.918	A
134	342	88	31.0	4.912	A
135	307	77	26.3	3.496	C
136	370	55	27.9	4.113	A
137	241	57	30.9	4.227	A
138	255	62	36.5	3.717	A
139	...	...	...	...	A
140	244	72	24.4	2.654	A
141	257	59	23.6	1.574	C
142	259	71	26.1	3.022	B
143	375	60	28.6	3.581	A
144	199	> 86	...	...	B
145	198	56	31.4	2.292	A
146	345	57	30.9	2.931	A
147	171	> 71	< 18.1	> 1.306	A
148	266	71	27.5	3.846	A
149	287	68	26.5	3.473	A
150	> 362	< 54	26.6	4.520	A
151	220	80	25.3	3.978	A
152	< 153	53	38.2	3.811	A
153	217	66	28.9	3.998	A
154	234	81	20.0	3.352	C
155	277	59	34.8	3.597	A
156	346	62	27.1	3.533	C
157	248	58	28.7	3.533	A
158	195	48	30.0	3.775	A
159	180	56	31.4	3.983	A
160	253	95	25.4	4.058	A
161	203	> 121	< 21.7	> 4.163	A
162	256	47	27.5	3.644	A
163	...	...	< 34.5	> 4.824	A
164	236	58	32.2	4.015	A

TABLE 2—*Continued*

Number	T(12/25) [K]	T(25/60) [K]	T(60/100) [K]	$-\log \tau_{100}$	Cloud group
165	...	...	< 15.5	> 1.821	A
166	> 692	< 44	32.5	4.536	A
167	< 211	60	24.8	3.997	A
168	< 149	56	24.9	3.432	A
169	< 175	51	27.3	3.679	A
170	283	94	29.6	4.001	A
171	262	64	25.9	3.638	A
172	260	69	23.9	3.437	A
173	207	82	25.2	3.783	A
174	264	69	28.2	4.060	A
175	279	60	27.9	3.561	A
176	< 206	50	28.2	3.967	A
177	241	73	22.8	3.563	A
178	286	80	20.8	3.279	A
179	284	57	29.6	3.969	A
180	232	71	22.4	3.189	A
181	161	62	25.2	3.399	A
182	246	67	23.1	3.617	A
183	303	63	24.9	3.530	A
184	317	60	25.6	3.560	A
185	< 139	74	21.8	3.590	A
186	205	78	19.5	3.120	A
187	207	77	19.0	2.943	A
188	246	100	18.9	2.352	C
189	...	...	...	...	C
190	268	60	27.2	3.998	A
191	213	65	22.9	3.578	A
192	282	62	25.5	2.999	C
193	233	64	23.4	3.045	A
194	...	< 54	23.9	3.509	A
195	270	64	22.6	3.384	A
196	314	61	23.7	3.284	A
197	< 307	57	30.2	4.228	A
198	577	57	25.1	3.666	A
199	311	61	25.7	3.676	A
200	269	60	24.2	3.544	A
201	218	62	29.1	4.391	A
202	208	67	22.7	3.183	A
203	269	67	25.0	3.265	A
204	< 105	90	16.9	2.735	A
205	180	66	31.4	3.580	C
206	256	74	23.6	3.248	A
207	382	66	25.4	3.880	A
208	190	74	22.4	3.389	A
209	289	76	26.8	3.891	A
210	277	68	23.1	3.601	A
211	237	80	23.5	3.569	C
212	254	67	27.1	4.087	A
213	< 240	65	23.3	3.329	A
214	248	63	23.6	3.241	A
215	277	60	21.6	3.082	C
216	204	78	26.9	3.651	C
217	249	64	31.4	3.224	A
218	200	79	22.3	3.468	A
219	229	67	23.4	4.235	A
220	269	86	20.9	3.981	A
221	267	71	26.0	4.044	A
222	357	74	20.8	3.708	A
223	313	> 177	< 14.5	> 3.018	A
224	224	71	25.8	3.760	C
225	226	67	16.6	2.483	C
226	> 473	...	< 11.2	> 0.817	A
227	393	77	14.2	2.069	A
228	396	65	23.8	4.006	A
229	254	72	23.2	3.675	A
230	220	55	27.2	3.812	A
231	274	78	21.6	3.381	A
232	163	83	25.8	3.796	A
233	173	55	37.6	4.577	A
234	< 204	50	18.3	2.839	A
235	326	78	> 46.2	< 5.993	A
236	223	> 172	...	...	A
237	356	51	40.6	5.029	A
238	275	58	19.5	3.160	A
239	266	80	32.2	5.444	...[c]
240	225	65	32.0	3.630	A
241	510	50	25.1	3.738	A
242	185	79	35.7	4.183	A
243	222	69	31.4	4.064	A
244	201	65	23.5	3.569	A
245	252	69	23.7	3.042	A
246	...	...	< 14.9	> 1.962	A
247	230	72	25.4	3.675	A
248	249	79	21.9	3.864	A

[a] Upper and lower limits indicate temperatures computed from a detection in one band and a 3 σ upper limit in the other band.
[b] Ellipses indicate upper limits for both bands, temperatures were not computed.
[c] CO not detected (three clouds) or not observed (one cloud).
[d] Not photometered.

weak UV component of the interstellar radiation field, penetrate deeply into the clouds? Two explanations are likely: either the clouds are very clumpy, or the dust grains are strongly forward-scattering for UV radiation. In the first case, the low area filling factor presented to the external UV radiation field could allow significant penetration into the globule bulk regions. We note, however, that although clumpiness has been demonstrated to exist in large molecular clouds (Snell *et al.* 1984; Schwartz *et al.* 1977), no corresponding evidence for small Bok globules exists. In the case of the forward scattering of the UV by dust grains, the effective penetration depth for UV could be much larger than for longer wavelengths. High albedo and large asymmetry phase factors for interstellar dust have been both observed (Witt and Lillie, 1973; Fitzgerald, Stevens, and Witt 1976) and modeled (Draine and Lee 1984) in the UV. Hence, significant forward scattering of the ISRF into the globule interiors is almost impossible to prevent. The presence of bright rims at optical wavelengths around one of these globules, CB 4, led Dickman and Clemens (1983) to conclude that the dust grains in that cloud were strongly forward-scattering at short wavelengths. This conclusion was also recently reached by Witt *et al.* (1990) from analysis of deep optical CCD images of CB 4, where they found $a(\lambda 4690) = 0.8$ and $g(\lambda 4690) = 0.7$. Thus, it is reasonable to expect the interiors of Bok globules to be filled with very blue or UV light which can be absorbed by small grains and lead to high non-equilibrium temperatures.

b) CO *Data Characteristics*

The histograms of Gaussian fitted ^{12}CO radiation temperature (antenna temperature corrected for main beam efficiency) and line width (FWHM) are shown in Figures 18 and 19, respectively. These figures are not significantly different in shape from those shown in CB, although there are roughly two-and-a-half times as many clouds in the current sample

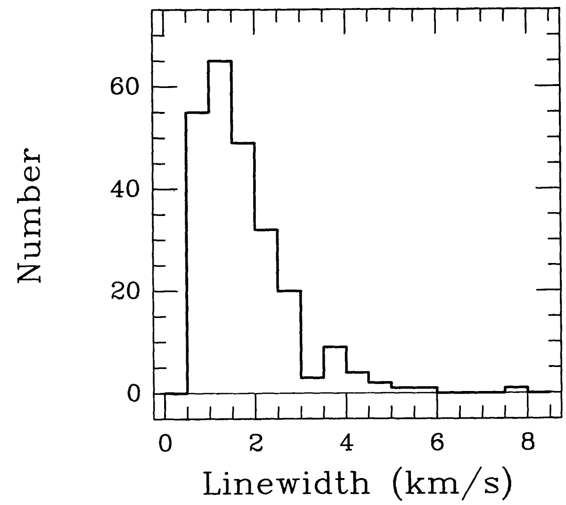

FIG. 19.—Histogram of ^{12}CO line widths (FWHM) for the CB clouds. The dominant peak in the distribution is at 1.25 km s^{-1}, while the mean and dispersion are 1.73 km s^{-1} and 1.01 km s^{-1}, respectively.

compared to those in CB. The histograms have means which are similar to the CB means, 4.89±2.91 K and 1.73±1.01 km s^{-1} for Figures 18 and 19, compared to 5.37±3.35 K and 1.70±1.06 km s^{-1} for CB. Figures 18 and 19 also show bifurcation into two components, as noted by CB.

When the CO temperatures and line widths of the globules are plotted as independent parameters, the cloud sample breaks up into three rough groups, as indicated by dashed lines in Figure 20. In this figure, the majority (74%) of the clouds fall near 4.5 K of radiation temperature (or roughly 8.5 K of

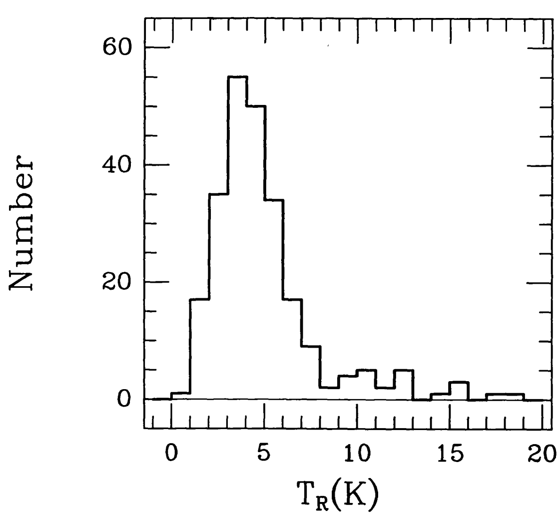

FIG. 18.—Histogram of ^{12}CO radiation temperatures (peak line antenna temperature corrected for telescope main beam efficiency) for the CB clouds. The dominant peak in the distribution is at 3.5 K, while the mean and dispersion are 4.89 and 2.91 K, respectively. The corresponding gas kinetic temperatures, for optically thick and thermalized lines, are 8.0, 9.6, and 3.2 K, respectively.

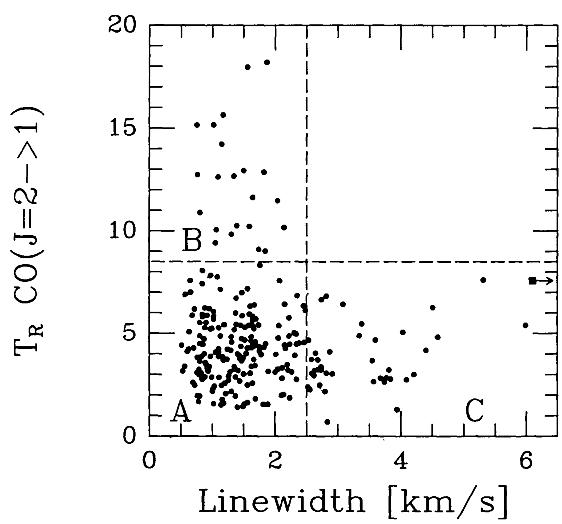

FIG. 20.—Comparison of CO peak line temperature and CO line width. Most (74%) of the clouds are in the lower left corner, where gas temperatures are cool, ~8.5 K, and turbulent gas motions are quiescent (subsonic, or only mildly transonic; A-type clouds). In the upper left quadrant, the clouds have unusually warm temperatures, but narrow lines (B-type clouds). In the lower right quadrant, the lines are quite broad, implying unusual dynamical activity, but the gas temperatures are cool (C-type clouds). There are no clouds in the upper right quadrant, which would characterize hot, dynamically active clouds.

kinetic temperature, if the CO line is optically thick and thermalized), and near 1–1.5 km s^{-1} line width, indicating that most of these clouds are cool and quiescent. Hereafter these clouds will be identified as belonging to group A. There are two much smaller groups of clouds which exhibit either warm and narrow lines (9% of the clouds; group B), or cool and wide lines (17% of the clouds; group C). In Table 2, the last column lists the group identification for each cloud. CB speculated that these three groups might form an evolutionary sequence and showed some evidence of temperature differences in the *IRAS* traced dust properties of the groups. The *IRAS* properties determined from the new co-added photometry are discussed in § IV, below.

c) *Correlations between IRAS and* CO *Properties*

Several simple comparisons between the properties of the globule dust characteristics and gas characteristics were performed to look for obvious correlations or interesting features. These included comparing the derived temperatures of the dust and gas, their implied column density estimates, and cross-correlations between temperature of one component and column density of the other component. In general, few trends were found, though there are several interesting departures from the gross lack of correlation. One possible explanation for the lack of correlations is that the area-averaged dust properties and the central, small-beam CO measurements sample quite different regions of the clouds. This issue must be resolved by more detailed observational data.

The first comparison was that between the dust temperature, as traced by the single-temperature blackbody fit to the 60

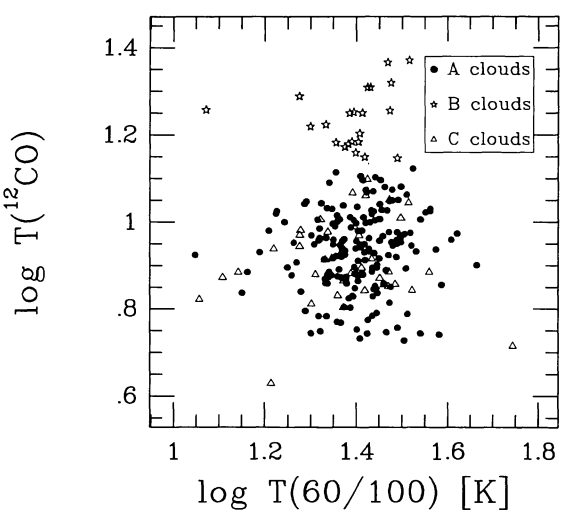

FIG. 21.—Distribution of CB clouds in the gas temperature–dust temperature plane. The gas temperature is traced by the derived kinetic temperature of the gas computed from the peak CO line radiation temperature. The dust temperature is derived from the *IRAS* 60 and 100 μm flux ratio, using the single-temperature model with a λ^{-1} emissivity. Different symbols denote the cloud types: *filled circles,* A; *open stars,* B; *open triangles,* C clouds (see legend). Most of the CB clouds show no correlation of their gas and dust temperatures (note the collection of points near T_{GAS} = 8.5 K, T_{DUST} = 25 K). There are some clouds which have warmer gas temperatures, but the same dust temperature as the bulk of the clouds. These clouds may be heated by an agent which can select the gas and not the dust.

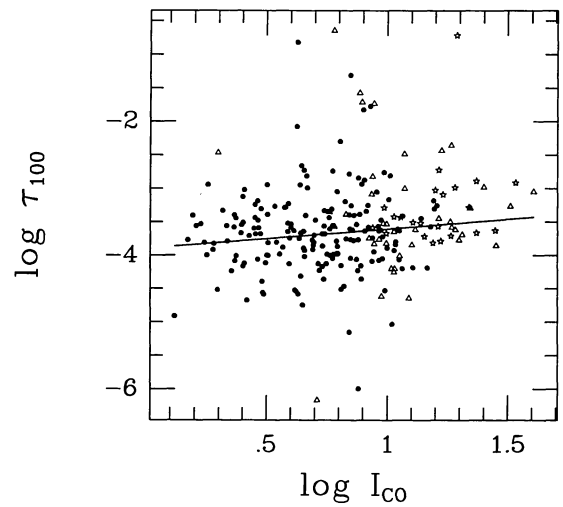

FIG. 22.—Distribution of CB clouds in the dust opacity–gas column density plane. The dust opacity is traced by the 100 μm opacity, derived from the single-temperature blackbody model and the 60 and 100 μm fluxes. The gas column density is represented by the integrated CO line strength I_{CO}, measured in K km s^{-1}. Symbols are as in Fig. 21. Ignoring the clouds with dust opacities greater than 10^{-2}, there is a weak correlation between the dust opacity and dust column density, with slope of 0.29±0.12. However, there is nothing like the unity slope correlation expected for well-mixed gas and dust in a fixed abundance ratio.

and 100 μm bands, and the gas temperature, as traced by the CO line radiation temperature, suitably converted to kinetic temperature. In all that follows, we will present only the λ^{-1} emissivity results, since the results for the λ^{-2} emissivity do not differ significantly. Figure 21 presents the distribution of globule temperatures in the log (T_{CO}) versus log ($T_{60/100}$) plane. The distribution of globules is roughly random, the only departure being the globules extending to high gas temperature (group B clouds). Ignoring that group of globules for the moment, the remaining collection of globules is distributed in a fairly Gaussian manner about T_{GAS} = 8.5 K, T_{DUST} = 25 K. The group of clouds with higher than average gas temperature does not seem to show significantly different dust temperatures compared to their cooler cousins. The gas heating in these clouds must either bypass the dust or not affect the smaller dust grains which emit at 60 and 100 μm. The lack of a correlation between the gas and dust temperature in all the clouds may be taken as evidence that the gas and dust systems are quite decoupled, as would be expected for the generally low volume densities of these clouds (Leung 1985).

Similarly, the column densities of gas and dust are compared in Figure 22, where log (τ_{100}) is plotted versus log (I_{CO}), the integrated CO line profile strength. The latter is a rather controversial estimator of the gas column density (e.g., Liszt 1982; Dickman 1988; Bloemen 1988), and, for these clouds, is likely only of limited utility. However, in the absence of a survey of the cloud gas properties in an optically thin gas tracer, the use of the optically thick CO line is expedient. If we ignore clouds with dust opacities greater than 0.01, and fit a line to the remaining points, a barely significant trend is found (linear correlation coefficient = 0.13). The trend has the form

$$\tau_{100} = 6 \times 10^{-5}(I_{CO})^{\alpha}, \quad (2)$$

where $\alpha = 0.29\pm0.15$, indicating that the dust opacity is only weakly dependent on the CO integrated intensity ($\approx$ gas column density). This weak dependence, and the very large amount of scatter about the best-fit relation, may indicate that cloud dust properties and gas properties are rather poorly related. Thus, Figure 22 would seem to show that the amount of dust incorporated into any particular Bok globule may be up to 10 times the amount of dust incorporated in a similar globule showing identical CO gas properties. However, it is also more than likely that the gas column density probe is less than robust, as already noted. It is equally true that the area-averaged dust opacity should be compared to the average gas column density over a similar angular area. Hence, although a strong gas-to-dust correlation does not appear in the data, hard conclusions regarding the cloud-to-cloud variation of the gas-to-dust ratio must await more complete data.

The similar correlations of temperature and column density are shown in Figure 23, where dust opacity is plotted versus gas temperature, and in Figure 24, where I_{CO} (gas column density) is plotted versus $T(60/100)$ (dust temperature). In Figure 23, the majority of clouds form a central blob near gas temperatures of 8.5 K and dust opacities of 5×10^{-4}. Again, as in the CO plot of Figure 20, the clouds also fall into two lesser groups defined by having warm gas temperatures and moderate dust opacity (group B clouds), and moderate gas temperatures and higher dust opacities. As expected, there is a high degree of correlation between the clouds in Figure 23, which are in extreme positions, and those extreme clouds in Figure 20. Figure 24 indicates no trend (linear correlation coefficient, $r \approx 0.05$) of integrated CO with dust temperature. There is a band of dust temperatures around 25 K which is almost perfectly vertical with I_{CO}, showing that the integrated *IRAS* colors for these clouds are not strongly affected by the gas column density.

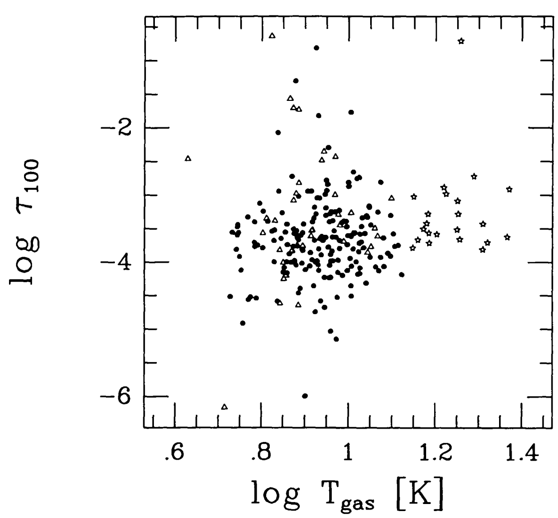

FIG. 23.—Distribution of CB clouds in the dust opacity–gas temperature plane. Symbols are as in Fig. 21. Most of the clouds inhabit the central collection of points in a fairly random fashion. There are two significant groupings of clouds away from the central collection: one characterized by higher dust opacities and the same gas temperatures as the clouds in the central collection, and the other to the right of the collection, where gas temperatures are higher, but dust opacities are about the same as the bulk of the clouds (group B clouds).

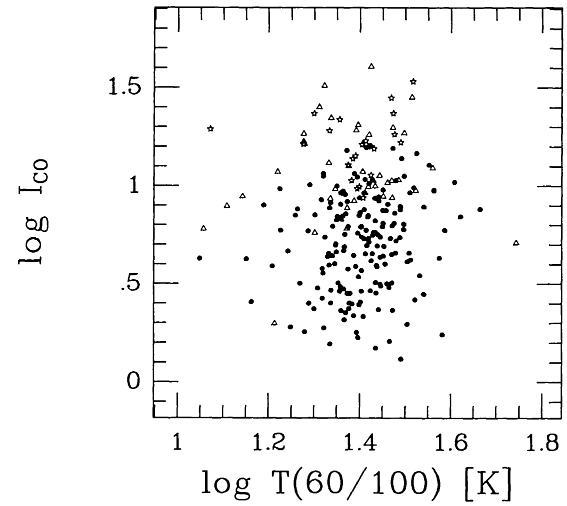

FIG. 24.—Distribution of CB clouds in the dust temperature–gas column density plane. Symbols are as in Fig. 21. A best-fit linear relation has a correlation coefficient of 0.05, indicating no significant correlation of the two quantities.

This does not indicate a lack of spatial variations *within* the clouds (something which is clearly seen; Leung 1985). Instead, it shows that, although the variation from cloud to cloud is large, the average inferred dust temperature is mostly unaffected.

IV. DERIVED PROPERTIES OF CB CLOUDS

The IRAS and CO properties of the three groups of clouds found in the CO analysis (quiescent, hot—narrow lines; cool—wide lines) are summarized in Table 3. In the table, the average CO temperatures and line widths are listed, as are the mean *IRAS* dust temperatures and opacities. The table seems to be dominated by similarities of the infrared properties of the three cloud groups.

Although the CO temperatures are different for at least two of the groups, the dust temperatures are remarkably similar for all three groups. This may be a consequence of the decoupling of the gas and dust heating and cooling processes, but leaves open the question of the nature of the extra gas heating seen for some of the clouds. Heating by radiation from nearby stars ought to be present more in the dust temperatures than in the gas temperatures. The gas is normally thought to be heated, at least to around 8–10 K, by cosmic-ray events (Goldsmith and Langer 1978). Perhaps the group B globules have strayed into a region of excess cosmic-ray flux, due to magnetic field focusing by shock waves or Parker instabilities. Alternatively, the gas in the clouds could be heated via gravitational collapse. However, both ideas seem *ad hoc* and require confirmation from other molecular temperature probes.

At this point, it is very difficult to find evidence to support the CB conjecture that the different cloud groups represent an evolutionary sequence. Instead, the *IRAS* temperature differences noted by CB seem more a result of the flux sensitivity limit of the PSC. When that flux limit is lowered by using the co-added matched aperture photometry, the FIR temperature differences between the A, B, and C group clouds are removed.

TABLE 3

SUMMARY OF GLOBULE GROUP PROPERTIES

Property	Group A	Group B	Group C
Number of clouds	179	22	41
$T_R(^{12}CO)$ [K]	4.2 ± 1.6[a]	12.4 ± 2.7	3.5 ± 1.5
$\Delta V(^{12}CO)$ [km s^{-1}]	1.4 ± 0.5	1.4 ± 0.4	3.5 ± 1.1
$T(12/25)$ [K]	252 ± 64	240 ± 92	267 ± 79
$T(25/60)$ [K]	71 ± 15	70 ± 8	70 ± 11
$T(60/100)$ [K]	26 ± 5	26 ± 4	26 ± 7
τ_{100}	−3.66 ± 0.63[b]	−3.27 ± 0.66[b]	−3.37 ± 0.95[b]
S_{IRAS} [Jy][c]	34 ± 19	104 ± 45	44 ± 27
Diameter: $(ab)^{0.5}$ [arcmin]	3.8 ± 1.8	5.5 ± 2.1	4.5 ± 2.3
L_{FIR} [$L_\odot$]	5.7 ± 3.1[b]	16.3 ± 7.5[b]	6.9 ± 4.4[b]
L_{FIR}/M_{CO} [$L_\odot/M_\odot$]	0.73 ± 0.41[b]	0.30 ± 0.16[b]	0.26 ± 0.18[b]

[a] All uncertainties listed represent the dispersion of the distributions and not the error of the mean.

[b] All L_{FIR}, τ_{100}, and L_{FIR}/M_{CO} values are calculated based on the logarithmic distributions.

[c] Sum of flux in all *IRAS* bands.

a) *Globule Heating by the ISRF*

Combination of the co-added *IRAS* matched aperture photometry and the CO data sets allows formation of a rough picture of the characteristics of Bok globules as a class of objects. In the CB paper, two arguments were advanced which favored a mean distance of about 600 pc for the clouds. If this distance is adopted for every cloud (a poor, but fair first approximation since no adequate direct distance estimates exist for any but a few of the clouds), then the *IRAS* luminosities for the clouds can be estimated. The *IRAS* co-added fluxes were summed and scaled to the 600 pc mean distance. The histogram of derived globule far-infrared luminosities is shown in Figure 25. The peak of the histogram is at 6 $L_\odot$ and the mean is 6.4 $L_\odot$. Note that the bolometric luminosity will be only marginally higher ($\leq$30%) because some of the dust emission is contained in wavelengths longer than the 100 μm channel of *IRAS* (see Myers *et al.* 1987). However, since the actual correction from L_{FIR} to L_{BOL} depends on knowledge of the dust grain size and temperature distributions, we limit our discussion to the observed *IRAS* far-infrared luminosity.

The heating of Bok globules is primarily done by the interstellar radiation field (ISRF) and by embedded protostars (if present). For optically opaque clouds, if the ISRF is fully thermalized by the Bok globules, the resulting far-infrared luminosity for our sample of clouds should be roughly

$$L_{FIR} \sim 23(D/4')^2 L_\odot \quad (3)$$

(Keene *et al.* 1980), where D is the diameter of the cloud in arcmin and 4′ is the mean of the optical sizes of the CB sample. The smallest CB clouds, those in the 1′–2′ range, dominate by number. For these clouds, Figure 25 indicates that the emergent luminosity ($\sim$6 $L_\odot$) balances the incident energy. Globules which depart from thermal equilibrium must have embedded sources of energy or be very optically thin.

If the CO spectral lines detected toward the cloud centers are presumed to be present over the entire area of the optically opaque cores cataloged by CB, than an estimate of the molecular mass in each cloud can be made. The CO integrated line strengths were converted into H_2 column densities using $X(CO) = 3.0 \times 10^{20}$ H_2 cm^{-2} (K km s^{-1})$^{-1}$ as a suitable conversion factor (Clemens, Sanders, and Scoville 1988, hereafter CSS). Again using 600 pc as the mean cloud distance, and correcting for the mass of He, Figure 26 shows the derived mass distribution of the CB clouds in units of $M_\odot$. The range of masses is from just under one solar mass to just over a couple of hundred solar masses. The peak of the histogram is near 15 $M_\odot$, with a mean of 11.4 $M_\odot$. For an average cloud diameter of 4′, at 600 pc this corresponds to a cloud radius of 0.35 pc, and, using the mean mass found, implies a mean density of 10^3 H_2 cm^{-3} for the clouds. This is in rough agreement with the density needed to excite CO.

Given the crude assumptions regarding distance and utility of integrated CO line strength as a column density indicator, a first guess at the ratio of L/M can be made. Figure 27 shows the distribution of L_{FIR}/M_{CO} for the CB clouds, derived from the *IRAS* luminosities and the CO cloud masses. The log-based mean is 0.5 $L_\odot/M_\odot$. This is quite below the range of 4–15 for active star-forming Giant Molecular Clouds (Scoville and Good 1987; Mooney and Solomon 1988) and the value of 2.8 for the mean of the Galactic disk (Scoville and Good 1987). Our value of 0.5 $L_\odot/M_\odot$ is quite close to the value computed for the Taurus region dark clouds B18 and Heiles's Cloud 2 (HCL 2), namely 0.26–0.3 $L_\odot/M_\odot$, by Snell, Heyer, and Schloerb (1989). Those authors argue that this low value of L/M is a *characteristic* of externally heated clouds. The somewhat larger Bok globule value found here is likely partially due to the warmer *IRAS* temperatures seen, relative to B18 and HCL 2. This may indicate that the UV component of the ISRF is better able to penetrate these fairly thin globules than the thicker Taurus clouds. Interestingly, some of the globules *do* have values of L/M beyond 10, and some have values smaller than 0.01.

Returning to Table 3, the average L_{FIR} and M_{CO} for the three different globule groups can be compared. In particular, the difference in the mean L_{FIR} between the different groups should be compared to the mean cloud sizes ($\sqrt{ab}$). Note that group B exhibits both the largest L_{FIR} and has clouds with larger average sizes. For these optically thin clouds, the luminosity at far-infrared wavelengths depends on the total volume of emissive material (assuming all other grain properties are the same). Hence, if the L_{FIR} of group B was higher than that of

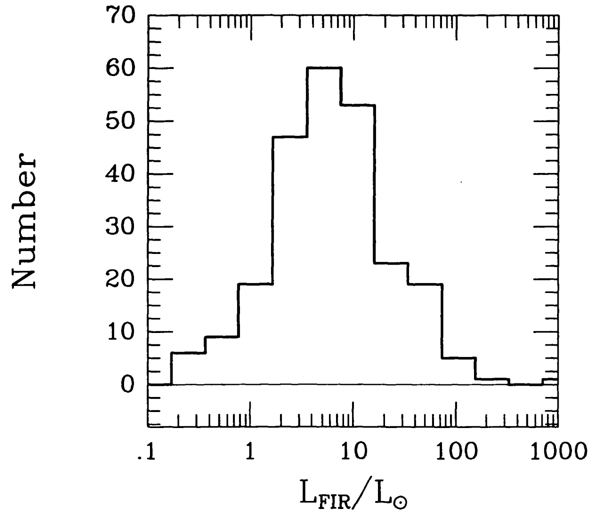

FIG. 25.—Histogram of far-infrared luminosities for the CB clouds. The luminosities were computed assuming a uniform distance of 600 pc to the globules and by summing the integrated flux seen in the four *IRAS* bands. The peak of the histogram is at 6 $L_\odot$, and the mean and dispersion are 6.4 and 3.8 $L_\odot$, respectively. The range of luminosities is from 0.5 to 300 $L_\odot$.

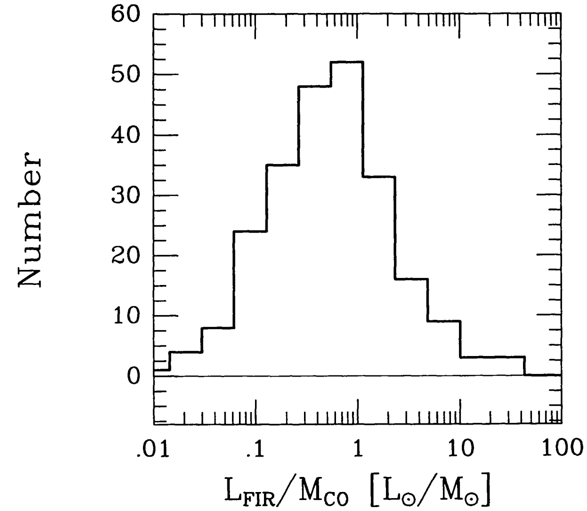

FIG. 27.—Histogram of the ratio of far-infrared luminosity to CO-traced cloud mass. The peak and median are at roughly 0.5 $L_\odot/M_\odot$. The range of ratios is 0.01 to 40 $L_\odot/M_\odot$.

group A by an amount in excess of that predicted by the larger group B cloud sizes, then one might implicate embedded stars as an extra luminosity source for group B. Surprisingly, if the luminosity is divided by the cube of the average cloud size, the specific luminosity is *highest* for group A, similar but lower for group B, and least for group C. This ordering is quite different from that proposed by CB for these groups. The clouds showing the warmest CO temperatures are the ones with the smallest far-infrared emission efficiency. Although this may indicate

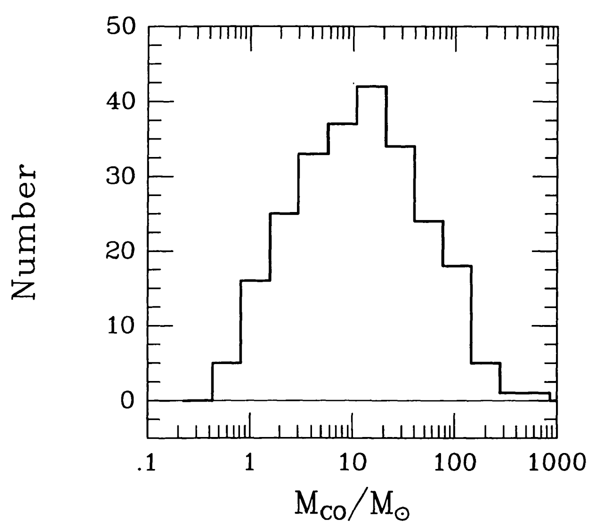

FIG. 26.—Histogram of the CO-based masses of the CB clouds. A uniform distance of 600 pc has been assumed, as has a conversion factor for the ratio of integrated CO emission to H_2 column density. The clouds were assumed to be emissive over their entire optically opaque cores with emission values identical to the observed center values. The mean cloud mass is 11.4 $M_\odot$, with a dispersion of 4.1 $M_\odot$. There are no clouds with masses smaller than 0.6 $M_\odot$, and only a couple of clouds exceed 100 $M_\odot$.

abnormal dust grain size distributions for the hot CO clouds, it seems unlikely that embedded stars are the source of these effects. This trend may also result from the gas-dust decoupling in the low densities of these clouds, previously discussed.

Alternatively, the correlation of higher FIR emissivity with smaller cloud size could indicate that the ISRF is only partially penetrating and heating the larger clouds. Since the emission seen at any wavelength is strongly biased toward regions of warmer temperatures, the cooler cores of the larger clouds could be missed. It is possible that L/M increases for very tiny Bok globules if their entire volume is actively absorbing the ISRF. Then the lower L/M values, which are virtually identical to those of B18 and HCL 2 in Taurus, could indicate that the cores of those larger globules are cooler and receive substantially less core heating from the ISRF. This interpretation could be tested by examining the spatial variation of *IRAS* emission within the photometric apertures.

One derived parameter which is often used to distinguish possible grain heating mechanisms is the intensity of 100 μm emission (I_{100} in MJy sr^{-1}) normalized by the column density of hydrogen atoms N_H (see Snell, Heyer, and Schloerb 1989). In Figure 28, we show the equivalent information for our Bok globules. In the Figure, the log of the integrated CO line strength is plotted versus the 100 μm intensity. The best-fit line is

$$\log(I_{CO}) = (1.103\pm0.064) + (0.198\pm0.045)\log(S_{100}/\text{area})\,. \quad (4)$$

Using the $X(\text{CO})$ from above, this can be rewritten in the conventional form:

$$I_{100}(\text{MJy sr}^{-1}) = 0.002\left(\frac{N_H}{10^{20}\text{ cm}^{-2}}\right)^5 . \quad (5)$$

Hence, the expected unity slope linear relation is not naturally present in the globule sample. However, if a unity slope *is*

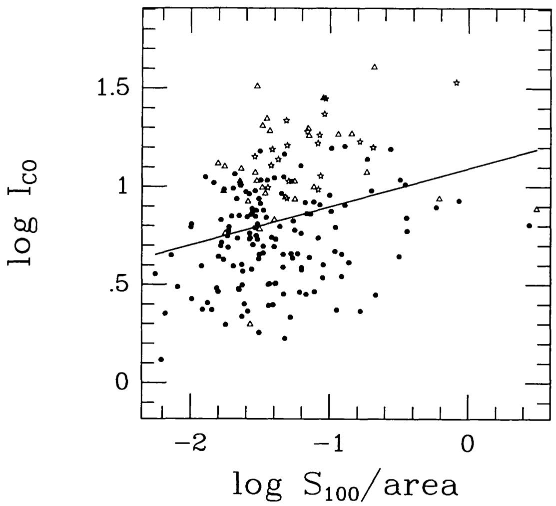

FIG. 28.—Plot of the integrated CO line strength I_{CO} vs. the 100 μm flux (S_{100}/area). The best-fit line has a slope of 0.198±0.045 and an intercept of 1.103±0.064. This Figure can be used to estimate the 100 μm dust flux yield per unit column density of H atoms.

fitted to the globule data points in Figure 28, the 100 μm yield is found to be about 0.003 MJy sr^{-1} per 10^{20} H atoms cm^{-2}. This value is 20–30 times lower than the value found by Snell, Heyer, and Schloerb (1989) for B18 and HCL 2. Either this factor is indicating the high level of ^{12}CO line opacity for these globules (quite possible), or that the linear relation imposed is not valid for a cloud-to-cloud comparison (also possible). Better estimates of N_H are clearly needed before the nature of this apparently low dust flux yield can be understood.

b) *Bok Globules as a Galactic Population*

Using the CB catalog and the results obtained above, we can make some estimates regarding the number and importance of Bok globules in our Galaxy. In all that follows, we will limit the possible range of properties by establishing strong lower and upper bounds for these properties. For the lower bounds, we assume that the CB catalog is 100% complete and that the volume density of such clouds is uniform (clouds pc^{-3}) from the Galactic center to a Galactic radius of 15 kpc, and that the globule volume density is equal to the local density. Thus, the lower limit to the number of clouds in the Galaxy is $[248/(600\text{pc})^2] \times (15{,}000 \text{ pc})^2 = 1.6 \times 10^5$.

However, the CB catalog is not complete. Whole regions of the sky were intentionally avoided, and the Galactic plane was severely underrepresented. Hence, for the upper bound, we estimate the CB completeness at, say, 33% and assume that the cloud number distribution with Galactic radius follows the Galactic molecular mass distribution (CSS) in showing a distinct peak near 5 kpc radius. In that case, the maximum number of Bok globules is $[248/(600 \text{ pc})^2] \times (15{,}000 \text{ pc})^2 \times 3 \times f$, where f is the ratio of mean molecular cloud density (clouds pc^{-3}) to the density seen locally. Using Figure 11 of CSS, we estimate $f = 1.4$. Hence, the maximum number of Bok globules in the Galaxy is roughly 6.5×10^5. This number is surely an overestimate because the mass spectrum of molecular clouds may be expected to change near spiral arms and in the molecular ring (Kwan and Valdes 1987). Hence, a reasonable guess to the number of isolated Bok globules can be computed as the logarithmic average of the upper and lower limits, and it is equal to 3.2×10^5 clouds.

Adopting the mean mass of 11 $M_\odot$ per cloud results in mass estimates between 1.8 and 7.4×10^6 $M_\odot$, or 0.05% to 0.2% of the 3.3×10^9 $M_\odot$ of molecular mass for the Galaxy (CSS). Similarly, using an average luminosity of 6 $L_\odot$, the total luminosity ranges from 1 to 4×10^6 $L_\odot$, or 0.007% to 0.03% of the 1.4×10^{10} $L_\odot$ of FIR luminosity estimated for our Galaxy (Sodrosky 1988).

Hence, Bok globules are not a particularly dominant constituent of the interstellar medium, either by mass or by luminosity. But equally, they cannot be an important reservoir for inactive molecular gas. For example, consider building one giant molecular cloud of 10^5 $M_\odot$ from the Galactic population of Bok globules. The low space density and low velocity dispersion (~5 km s^{-1}; Clemens 1985) conspire to cause the minimum growth time to be a few Hubble times.

V. SUMMARY

The entire sample (248 objects) of small molecular clouds cataloged by Clemens and Barvainis (1988) has been probed using deep, co-added *IRAS* survey data analysis and using ^{12}CO spectroscopy.

The chief findings of this effort include the following:

1. The technique of matched aperture photometry of the *IRAS* image data returns superior flux measurements of small clouds compared to the PSC-listed fluxes. Additionally, there is no confusion regarding the lack of a pointlike nature to the emission.

2. Co-added *IRAS* survey image analysis lowered the detection threshold below the flux level for these clouds. Thermal emission from virtually all of the clouds was detected in all of the *IRAS* bands.

3. The far-infrared colors are similar to those found for other amorphous constituents of the Galaxy. The mean 12/25 μm color, log (S_{12}/S_{25}), found was 0.01 (~250 K), the mean 25/60 μm color found was 0.68 (~70 K), and the mean 60/100 μm color found was 0.70 (~26 K).

4. The mean dust optical depth found at 100 μm was 0.00025, representing no more than ~10% of the expected dust opacity. Hence, as seen in other studies, the bulk of the dust mass was colder than 30 K and thereby invisible to *IRAS*.

5. The *IRAS* colors and fluxes are such that these clouds cannot be selected or distinguished from other Galactic molecular clouds in FIR two-color diagrams.

6. We find a very strong anticorrelation between dust optical depth and 60/100 μm color temperature. The slope of the correlation is softer than that produced by changes in the 60 μm emission level alone.

7. The ^{12}CO spectroscopy detected 244 of the clouds, confirming the molecular nature of this optically selected sample.

8. The ^{12}CO properties are virtually identical to those found by CB, including the separation of the cloud sample into quiescent, hot, and turbulent subsamples of clouds.

9. We searched for correlations between the dust and gas properties of these clouds. We found no strong trends, and a great deal of scatter in the cloud-to-cloud properties at least in

part due to our crude assumptions needed to convert observed fluxes to temperatures and opacities. We conclude that the dust and gas systems in these clouds are very poorly coupled (Leung 1985), if at all.

10. We find that the mean far-infrared luminosity of the sample is around 6.4 $L_{\odot}$, almost exactly the value expected if the ISRF is the dominant heat source.

11. The mean cloud mass is around 11 $M_{\odot}$, the radius is around 0.35 pc, and the density is around 10^3 H_2 cm^{-3}.

12. The mean L_{FIR}/M_{CO} for the sample is 0.5 $L_{\odot}/M_{\odot}$, with a full range spanning 0.01 to almost 100 $L_{\odot}/M_{\odot}$.

13. We are unable to confirm the possible evolutionary sequence within this cloud sample proposed by CB. The seemingly CO active clouds exhibit *IRAS* traced specific luminosities which are smaller than the quiescent cloud sample.

14. Upper and lower limits for the number of these clouds in the Galaxy are 1.6×10^5 and 6.5×10^5.

15. Combining these numbers with the average mass and luminosity yields a total Galactic mass in Bok globules of about 3.5×10^6 $M_{\odot}$ and a total luminosity of about 2×10^6 $L_{\odot}$.

This work has been especially aided by the assistance of Gaylin Laughlin (IPAC), Larry Strom and Neal Evans (both of the University of Texas), R. Barvainis (Haystack Observatory), and R. Leach (SDSU). Cathy Clemens performed much of the observing during the 1988 MWO run. A careful reading by a particularly conscientious referee resulted in a substantially improved paper. This research has been partially supported by NASA-ADP and *IRAS*-GI awards (including NAS7-918 and NAG51160) and by start-up funds from the Office of the Dean, College of Liberal Arts, Boston University, all to D.C. Support from the Gulbenkian Foundation to J.L.Y. in the form of a fellowship is gratefully acknowledged.

APPENDIX

LOOKUP TABLE FOR FLUX RATIO TO TEMPERATURE CONVERSIONS OF *IRAS* DATA

The lookup table in the *IRAS Explanatory Supplement,* for converting flux ratios seen between neighboring *IRAS* bands, has limited utility when cold clouds are being considered. That table does not extend below 40 K, does not include emissivity effects, and has large steps between the tabulated temperatures. We have computed our own lookup tables, based on the average wavelength responses of the *IRAS* detectors as shown in Figure 2 of Neugebauer *et al.* (1984). These responses have been convolved with the fluxes expected from blackbodies modified by emissivity laws of the form λ^{-1} and λ^{-2} to yield flux ratios and color corrections for each band.

We chose to interpolate the curves of detector response rather than use the tabulated detector responses in the *IRAS Explanatory Supplement.* The reason for this choice was that the tabulations were rather coarse, and, in the case of very cold clouds, this can affect the derived flux ratios. For warmer temperatures, this effect is not particularly important. The algorithm used has been supplied to IPAC, and can be obtained from that facility.

We list below four tables (Tables 4–7): two for each emissivity, and within each emissivity, one with 1 K steps appropriate for cold temperatures (and especially the 60 and 100 μm bands) and one with 10 K steps appropriate for warmer temperatures (and especially the 12 and 25 μm bands). Our tables agree with the *Supplement* table for the case of zero in the exponent of the emissivity term, but extend to lower temperatures, at finer temperature spacings, and include the effects of emissivities. In the tables, the *K* factors are the flux correction factors ("color corrections") for each band and temperature.

Tables 4–7 follow.

TABLE 4

λ^{-1} EMISSIVITY, LOW TEMPERATURES

T (K)	K_{12}	K_{25}	K_{60}	K_{100}	$log(S_{12}/S_{25})$	$log(S_{25}/S_{60})$	$log(S_{60}/S_{100})$
6	...	...	340.1098	5.0108	...	...	−4.2240
7	...	...	90.9622	3.0099	...	...	−3.5835
8	...	...	35.3805	2.1504	...	...	−3.1037
9	...	...	17.5307	1.7090	...	...	−2.7303
10	...	...	10.2419	1.4544	...	...	−2.4308
11	...	...	6.7243	1.2957	...	...	−2.1846
12	...	...	4.8082	1.1912	...	...	−1.9781
13	...	43.3588	3.6658	1.1197	...	−8.6220	−1.8021
14	...	27.3679	2.9357	1.0696	...	−7.9242	−1.6497
15	...	18.4943	2.4432	1.0338	...	−7.3204	−1.5163
16	...	13.2038	2.0964	1.0080	...	−6.7927	−1.3983
17	...	9.8597	1.8436	0.9894	...	−6.3277	−1.2929
18	...	7.6413	1.6541	0.9760	...	−5.9148	−1.1980
19	...	6.1089	1.5087	0.9666	...	−5.5457	−1.1120
20	...	5.0137	1.3951	0.9602	...	−5.2138	−1.0336
21	...	4.2079	1.3049	0.9560	...	−4.9137	−0.9617
22	...	3.5999	1.2323	0.9536	...	−4.6411	−0.8955
23	...	3.1311	1.1734	0.9526	...	−4.3922	−0.8341
24	...	2.7629	1.1250	0.9526	...	−4.1642	−0.7772
25	228.0986	2.4689	1.0852	0.9535	−7.5905	−3.9544	−0.7241
26	164.4482	2.2306	1.0522	0.9551	−7.2720	−3.7607	−0.6745
27	121.8027	2.0351	1.0247	0.9571	−6.9768	−3.5814	−0.6280
28	92.3616	1.8729	1.0018	0.9596	−6.7027	−3.4148	−0.5842
29	71.5154	1.7369	0.9826	0.9624	−6.4476	−3.2596	−0.5430
30	56.4202	1.6218	0.9667	0.9654	−6.2095	−3.1147	−0.5041
31	45.2671	1.5238	0.9534	0.9685	−5.9869	−2.9791	−0.4673
32	36.8750	1.4396	0.9425	0.9719	−5.7783	−2.8518	−0.4324
33	30.4553	1.3668	0.9335	0.9753	−5.5825	−2.7322	−0.3993
34	25.4700	1.3036	0.9261	0.9787	−5.3982	−2.6194	−0.3678
35	21.5449	1.2484	0.9203	0.9822	−5.2246	−2.5130	−0.3378
36	18.4156	1.2000	0.9156	0.9857	−5.0606	−2.4124	−0.3093
37	15.8917	1.1573	0.9121	0.9892	−4.9056	−2.3171	−0.2820
38	13.8344	1.1196	0.9095	0.9926	−4.7589	−2.2267	−0.2560
39	12.1408	1.0862	0.9078	0.9961	−4.6197	−2.1408	−0.2311
40	10.7340	1.0564	0.9068	0.9995	−4.4875	−2.0590	−0.2073
41	9.5556	1.0299	0.9064	1.0028	−4.3619	−1.9812	−0.1845
42	8.5608	1.0063	0.9067	1.0061	−4.2423	−1.9069	−0.1626
43	7.7149	0.9851	0.9074	1.0093	−4.1283	−1.8359	−0.1416
44	6.9907	0.9661	0.9085	1.0125	−4.0196	−1.7681	−0.1214
45	6.3669	0.9491	0.9101	1.0156	−3.9157	−1.7032	−0.1020
46	5.8263	0.9338	0.9120	1.0186	−3.8164	−1.6409	−0.0833
47	5.3553	0.9201	0.9142	1.0216	−3.7213	−1.5812	−0.0654
48	4.9428	0.9078	0.9167	1.0245	−3.6302	−1.5239	−0.0481
49	4.5798	0.8967	0.9194	1.0274	−3.5429	−1.4689	−0.0314
50	4.2589	0.8868	0.9223	1.0301	−3.4591	−1.4159	−0.0153
51	3.9740	0.8779	0.9254	1.0328	−3.3786	−1.3649	0.0002
52	3.7201	0.8699	0.9287	1.0355	−3.3012	−1.3158	0.0151
53	3.4930	0.8628	0.9321	1.0381	−3.2267	−1.2685	0.0296
54	3.2890	0.8565	0.9356	1.0406	−3.1551	−1.2228	0.0436
55	3.1052	0.8508	0.9393	1.0430	−3.0860	−1.1787	0.0571
56	2.9392	0.8458	0.9430	1.0454	−3.0194	−1.1361	0.0701
57	2.7886	0.8414	0.9468	1.0478	−2.9551	−1.0949	0.0828
58	2.6518	0.8376	0.9507	1.0500	−2.8931	−1.0550	0.0950
59	2.5271	0.8342	0.9546	1.0522	−2.8331	−1.0165	0.1069
60	2.4131	0.8313	0.9586	1.0544	−2.7752	−0.9791	0.1184
61	2.3087	0.8288	0.9626	1.0565	−2.7191	−0.9429	0.1295
62	2.2128	0.8268	0.9667	1.0586	−2.6649	−0.9079	0.1403
63	2.1246	0.8251	0.9707	1.0606	−2.6123	−0.8739	0.1508
64	2.0433	0.8237	0.9748	1.0625	−2.5614	−0.8408	0.1610
65	1.9682	0.8226	0.9789	1.0644	−2.5120	−0.8088	0.1708
66	1.8987	0.8219	0.9831	1.0663	−2.4641	−0.7777	0.1804
67	1.8342	0.8213	0.9872	1.0681	−2.4176	−0.7474	0.1898
68	1.7743	0.8211	0.9913	1.0699	−2.3725	−0.7180	0.1988
69	1.7186	0.8211	0.9954	1.0716	−2.3286	−0.6894	0.2076
70	1.6668	0.8213	0.9994	1.0733	−2.2860	−0.6616	0.2162
71	1.6183	0.8217	1.0035	1.0750	−2.2445	−0.6345	0.2245
72	1.5731	0.8223	1.0076	1.0766	−2.2042	−0.6081	0.2326
73	1.5308	0.8230	1.0116	1.0781	−2.1649	−0.5825	0.2405
74	1.4912	0.8240	1.0156	1.0797	−2.1267	−0.5575	0.2482
75	1.4540	0.8251	1.0196	1.0812	−2.0895	−0.5331	0.2556
76	1.4191	0.8263	1.0236	1.0826	−2.0532	−0.5093	0.2629
77	1.3863	0.8277	1.0275	1.0841	−2.0178	−0.4861	0.2700
78	1.3554	0.8291	1.0314	1.0855	−1.9833	−0.4635	0.2769
79	1.3264	0.8308	1.0353	1.0868	−1.9497	−0.4415	0.2837
80	1.2990	0.8325	1.0391	1.0882	−1.9168	−0.4199	0.2903
81	1.2731	0.8343	1.0429	1.0895	−1.8847	−0.3989	0.2967
82	1.2487	0.8362	1.0467	1.0908	−1.8534	−0.3783	0.3029
83	1.2256	0.8382	1.0504	1.0920	−1.8228	−0.3583	0.3091
84	1.2038	0.8403	1.0541	1.0932	−1.7929	−0.3387	0.3150
85	1.1831	0.8425	1.0578	1.0944	−1.7636	−0.3195	0.3209
86	1.1636	0.8447	1.0614	1.0956	−1.7350	−0.3008	0.3265
87	1.1450	0.8470	1.0650	1.0967	−1.7070	−0.2825	0.3321
88	1.1274	0.8494	1.0686	1.0979	−1.6796	−0.2646	0.3375
89	1.1108	0.8518	1.0721	1.0990	−1.6528	−0.2470	0.3428
90	1.0949	0.8543	1.0756	1.1000	−1.6266	−0.2299	0.3480
91	1.0799	0.8568	1.0791	1.1011	−1.6009	−0.2131	0.3531
92	1.0656	0.8594	1.0825	1.1021	−1.5757	−0.1967	0.3581
93	1.0520	0.8620	1.0858	1.1031	−1.5510	−0.1806	0.3629
94	1.0391	0.8647	1.0892	1.1041	−1.5268	−0.1648	0.3677
95	1.0268	0.8674	1.0925	1.1051	−1.5031	−0.1494	0.3723
96	1.0151	0.8701	1.0957	1.1060	−1.4798	−0.1343	0.3769
97	1.0039	0.8729	1.0990	1.1070	−1.4569	−0.1194	0.3813
98	0.9933	0.8757	1.1022	1.1079	−1.4345	−0.1049	0.3857
99	0.9832	0.8786	1.1053	1.1088	−1.4126	−0.0907	0.3899
100	0.9735	0.8814	1.1084	1.1097	−1.3910	−0.0767	0.3941

TABLE 5

λ^{-1} Emissivity, High Temperatures

T (K)	K_{12}	K_{25}	K_{60}	K_{100}	$log(S_{12}/S_{25})$	$log(S_{25}/S_{60})$	$log(S_{60}/S_{100})$
110	0.8987	0.9110	1.1377	1.1176	−1.1948	0.0491	0.4316
120	0.8522	0.9413	1.1636	1.1242	−1.0282	0.1540	0.4626
130	0.8241	0.9713	1.1867	1.1298	−0.8844	0.2428	0.4887
140	0.8086	1.0005	1.2072	1.1346	−0.7587	0.3186	0.5108
150	0.8019	1.0285	1.2255	1.1388	−0.6475	0.3841	0.5298
160	0.8016	1.0552	1.2419	1.1424	−0.5485	0.4411	0.5462
170	0.8060	1.0804	1.2566	1.1456	−0.4596	0.4911	0.5606
180	0.8139	1.1042	1.2699	1.1484	−0.3794	0.5352	0.5733
190	0.8244	1.1266	1.2819	1.1510	−0.3065	0.5744	0.5846
200	0.8368	1.1476	1.2929	1.1532	−0.2401	0.6094	0.5947
210	0.8507	1.1674	1.3029	1.1553	−0.1793	0.6408	0.6037
220	0.8658	1.1859	1.3120	1.1571	−0.1235	0.6692	0.6118
230	0.8816	1.2033	1.3204	1.1588	−0.0721	0.6949	0.6192
240	0.8979	1.2196	1.3282	1.1604	−0.0246	0.7183	0.6260
250	0.9146	1.2349	1.3353	1.1618	0.0193	0.7396	0.6321
260	0.9315	1.2493	1.3419	1.1631	0.0601	0.7592	0.6378
270	0.9485	1.2629	1.3481	1.1643	0.0981	0.7772	0.6430
280	0.9654	1.2757	1.3538	1.1654	0.1335	0.7937	0.6478
290	0.9823	1.2877	1.3591	1.1664	0.1665	0.8090	0.6523
300	0.9990	1.2990	1.3641	1.1674	0.1975	0.8232	0.6564
310	1.0155	1.3097	1.3688	1.1683	0.2265	0.8364	0.6602
320	1.0317	1.3199	1.3731	1.1691	0.2537	0.8487	0.6638
330	1.0477	1.3295	1.3773	1.1699	0.2792	0.8602	0.6672
340	1.0634	1.3385	1.3811	1.1707	0.3033	0.8709	0.6704
350	1.0787	1.3472	1.3848	1.1714	0.3260	0.8810	0.6733
360	1.0937	1.3553	1.3882	1.1720	0.3475	0.8904	0.6761
370	1.1084	1.3631	1.3915	1.1726	0.3677	0.8993	0.6787
380	1.1227	1.3705	1.3946	1.1732	0.3869	0.9076	0.6812
390	1.1367	1.3775	1.3976	1.1738	0.4051	0.9155	0.6836
400	1.1503	1.3842	1.4004	1.1743	0.4223	0.9230	0.6858
410	1.1636	1.3906	1.4030	1.1748	0.4387	0.9301	0.6879
420	1.1765	1.3967	1.4055	1.1753	0.4543	0.9367	0.6899
430	1.1891	1.4025	1.4080	1.1757	0.4691	0.9431	0.6918
440	1.2013	1.4081	1.4103	1.1762	0.4832	0.9491	0.6936
450	1.2133	1.4135	1.4125	1.1766	0.4967	0.9549	0.6953
460	1.2249	1.4186	1.4146	1.1770	0.5095	0.9603	0.6970
470	1.2362	1.4235	1.4166	1.1774	0.5218	0.9655	0.6986
480	1.2471	1.4282	1.4185	1.1777	0.5335	0.9705	0.7001
490	1.2578	1.4327	1.4204	1.1781	0.5447	0.9752	0.7015
500	1.2682	1.4370	1.4221	1.1784	0.5555	0.9798	0.7029
510	1.2783	1.4412	1.4238	1.1787	0.5658	0.9841	0.7042
520	1.2882	1.4452	1.4255	1.1790	0.5756	0.9883	0.7055
530	1.2977	1.4491	1.4270	1.1793	0.5851	0.9923	0.7067
540	1.3070	1.4528	1.4286	1.1796	0.5942	0.9961	0.7079
550	1.3161	1.4564	1.4300	1.1799	0.6029	0.9998	0.7090
560	1.3249	1.4598	1.4314	1.1801	0.6114	1.0033	0.7101
570	1.3335	1.4631	1.4328	1.1804	0.6194	1.0067	0.7111
580	1.3419	1.4664	1.4341	1.1806	0.6272	1.0100	0.7121
590	1.3500	1.4695	1.4354	1.1809	0.6347	1.0132	0.7131
600	1.3579	1.4725	1.4366	1.1811	0.6420	1.0162	0.7140
610	1.3656	1.4754	1.4378	1.1813	0.6490	1.0191	0.7149
620	1.3732	1.4782	1.4389	1.1815	0.6557	1.0220	0.7158
630	1.3805	1.4809	1.4400	1.1817	0.6622	1.0247	0.7167
640	1.3876	1.4836	1.4411	1.1819	0.6685	1.0273	0.7175
650	1.3946	1.4861	1.4421	1.1821	0.6745	1.0299	0.7183
660	1.4013	1.4886	1.4432	1.1823	0.6804	1.0323	0.7190
670	1.4080	1.4910	1.4441	1.1825	0.6861	1.0347	0.7198
680	1.4144	1.4933	1.4451	1.1827	0.6916	1.0370	0.7205
690	1.4207	1.4956	1.4460	1.1829	0.6969	1.0393	0.7212
700	1.4268	1.4978	1.4469	1.1830	0.7021	1.0415	0.7219
710	1.4328	1.4999	1.4478	1.1832	0.7071	1.0436	0.7225
720	1.4386	1.5020	1.4486	1.1833	0.7119	1.0456	0.7232
730	1.4443	1.5040	1.4494	1.1835	0.7167	1.0476	0.7238
740	1.4499	1.5060	1.4502	1.1836	0.7212	1.0495	0.7244
750	1.4553	1.5079	1.4510	1.1838	0.7257	1.0514	0.7250
760	1.4607	1.5097	1.4518	1.1839	0.7300	1.0532	0.7256
770	1.4658	1.5115	1.4525	1.1841	0.7342	1.0549	0.7261
780	1.4709	1.5133	1.4532	1.1842	0.7382	1.0567	0.7267
790	1.4759	1.5150	1.4539	1.1843	0.7422	1.0583	0.7272
800	1.4807	1.5167	1.4546	1.1844	0.7460	1.0600	0.7277
810	1.4854	1.5183	1.4553	1.1846	0.7498	1.0615	0.7282
820	1.4901	1.5199	1.4559	1.1847	0.7534	1.0631	0.7287
830	1.4946	1.5214	1.4565	1.1848	0.7570	1.0646	0.7292
840	1.4990	1.5230	1.4572	1.1849	0.7604	1.0660	0.7296
850	1.5034	1.5244	1.4578	1.1850	0.7638	1.0675	0.7301
860	1.5076	1.5259	1.4583	1.1851	0.7671	1.0689	0.7305
870	1.5117	1.5273	1.4589	1.1852	0.7703	1.0702	0.7309
880	1.5158	1.5286	1.4595	1.1854	0.7734	1.0715	0.7314
890	1.5198	1.5300	1.4600	1.1855	0.7764	1.0728	0.7318
900	1.5237	1.5313	1.4606	1.1856	0.7794	1.0741	0.7322
910	1.5275	1.5326	1.4611	1.1856	0.7823	1.0753	0.7326
920	1.5312	1.5338	1.4616	1.1857	0.7851	1.0765	0.7330
930	1.5349	1.5351	1.4621	1.1858	0.7879	1.0777	0.7333
940	1.5385	1.5363	1.4626	1.1859	0.7906	1.0788	0.7337
950	1.5420	1.5374	1.4631	1.1860	0.7932	1.0800	0.7341
960	1.5455	1.5386	1.4635	1.1861	0.7958	1.0811	0.7344
970	1.5488	1.5397	1.4640	1.1862	0.7983	1.0821	0.7348
980	1.5522	1.5408	1.4645	1.1863	0.8008	1.0832	0.7351
990	1.5554	1.5419	1.4649	1.1864	0.8032	1.0842	0.7354
1000	1.5586	1.5429	1.4653	1.1864	0.8055	1.0852	0.7357

TABLE 6

λ^{-2} EMISSIVITY, LOW TEMPERATURES

T (K)	K_{12}	K_{25}	K_{60}	K_{100}	$log(S_{12}/S_{25})$	$log(S_{25}/S_{60})$	$log(S_{60}/S_{100})$
6	...	...	259.7608	4.2196	...	...	−4.0445
7	...	...	70.4645	2.5914	...	...	−3.4075
8	...	...	27.7608	1.8875	...	...	−2.9305
9	...	...	13.9189	1.5255	...	...	−2.5593
10	...	...	8.2227	1.3175	...	...	−2.2613
11	...	...	5.4558	1.1889	...	...	−2.0162
12	...	...	3.9408	1.1056	...	...	−1.8103
13	...	37.0004	3.0338	1.0500	...	−8.2285	−1.6344
14	...	23.4213	2.4526	1.0122	...	−7.5336	−1.4820
15	...	15.8732	2.0599	0.9864	...	−6.9324	−1.3482
16	...	11.3652	1.7832	0.9691	...	−6.4074	−1.2296
17	...	8.5113	1.5818	0.9577	...	−5.9448	−1.1234
18	...	6.6155	1.4312	0.9506	...	−5.5343	−1.0276
19	...	5.3044	1.3162	0.9468	...	−5.1676	−0.9405
20	...	4.3662	1.2269	0.9455	...	−4.8379	−0.8608
21	...	3.6753	1.1566	0.9459	...	−4.5399	−0.7876
22	...	3.1537	1.1007	0.9477	...	−4.2693	−0.7200
23	...	2.7513	1.0559	0.9506	...	−4.0224	−0.6572
24	...	2.4351	1.0198	0.9543	...	−3.7961	−0.5987
25	187.7560	2.1826	0.9907	0.9585	−7.3028	−3.5881	−0.5441
26	135.4861	1.9780	0.9672	0.9632	−6.9852	−3.3961	−0.4929
27	100.4875	1.8103	0.9483	0.9683	−6.6907	−3.2184	−0.4448
28	76.3082	1.6711	0.9331	0.9736	−6.4174	−3.0533	−0.3995
29	59.1709	1.5546	0.9212	0.9790	−6.1630	−2.8995	−0.3566
30	46.7487	1.4561	0.9118	0.9845	−5.9256	−2.7560	−0.3161
31	37.5613	1.3724	0.9048	0.9901	−5.7038	−2.6216	−0.2778
32	30.6415	1.3006	0.8996	0.9957	−5.4959	−2.4955	−0.2413
33	25.3431	1.2388	0.8960	1.0013	−5.3008	−2.3769	−0.2066
34	21.2246	1.1852	0.8939	1.0068	−5.1173	−2.2652	−0.1736
35	17.9792	1.1385	0.8930	1.0123	−4.9444	−2.1597	−0.1422
36	15.3894	1.0978	0.8931	1.0177	−4.7812	−2.0600	−0.1122
37	13.2989	1.0620	0.8941	1.0230	−4.6269	−1.9655	−0.0835
38	11.5934	1.0306	0.8959	1.0282	−4.4809	−1.8759	−0.0560
39	10.1884	1.0029	0.8984	1.0333	−4.3424	−1.7907	−0.0297
40	9.0204	0.9785	0.9016	1.0383	−4.2110	−1.7096	−0.0045
41	8.0413	0.9568	0.9052	1.0431	−4.0861	−1.6323	0.0196
42	7.2142	0.9377	0.9093	1.0479	−3.9672	−1.5586	0.0428
43	6.5104	0.9207	0.9138	1.0526	−3.8539	−1.4881	0.0651
44	5.9075	0.9057	0.9187	1.0571	−3.7459	−1.4207	0.0865
45	5.3879	0.8924	0.9238	1.0615	−3.6427	−1.3562	0.1072
46	4.9373	0.8806	0.9293	1.0658	−3.5440	−1.2944	0.1270
47	4.5445	0.8702	0.9350	1.0700	−3.4496	−1.2350	0.1461
48	4.2003	0.8610	0.9408	1.0741	−3.3592	−1.1780	0.1645
49	3.8973	0.8530	0.9469	1.0781	−3.2725	−1.1232	0.1823
50	3.6293	0.8460	0.9531	1.0820	−3.1893	−1.0704	0.1995
51	3.3913	0.8398	0.9594	1.0857	−3.1094	−1.0196	0.2160
52	3.1791	0.8345	0.9659	1.0894	−3.0327	−0.9707	0.2320
53	2.9892	0.8300	0.9724	1.0930	−2.9588	−0.9235	0.2474
54	2.8186	0.8261	0.9790	1.0964	−2.8877	−0.8779	0.2624
55	2.6649	0.8229	0.9856	1.0998	−2.8192	−0.8339	0.2768
56	2.5260	0.8202	0.9923	1.1031	−2.7531	−0.7913	0.2908
57	2.4000	0.8181	0.9991	1.1063	−2.6894	−0.7502	0.3044
58	2.2855	0.8165	1.0058	1.1094	−2.6278	−0.7104	0.3175
59	2.1812	0.8153	1.0126	1.1124	−2.5684	−0.6718	0.3302
60	2.0858	0.8145	1.0194	1.1154	−2.5109	−0.6345	0.3425
61	1.9984	0.8141	1.0261	1.1183	−2.4553	−0.5983	0.3545
62	1.9182	0.8141	1.0329	1.1211	−2.4014	−0.5631	0.3660
63	1.8445	0.8144	1.0396	1.1238	−2.3493	−0.5291	0.3773
64	1.7765	0.8150	1.0464	1.1264	−2.2988	−0.4960	0.3882
65	1.7137	0.8159	1.0531	1.1290	−2.2498	−0.4639	0.3988
66	1.6556	0.8170	1.0597	1.1316	−2.2023	−0.4326	0.4091
67	1.6017	0.8184	1.0664	1.1340	−2.1561	−0.4023	0.4191
68	1.5518	0.8200	1.0729	1.1364	−2.1113	−0.3728	0.4289
69	1.5053	0.8218	1.0795	1.1387	−2.0678	−0.3441	0.4383
70	1.4620	0.8238	1.0860	1.1410	−2.0255	−0.3161	0.4475
71	1.4217	0.8260	1.0925	1.1432	−1.9843	−0.2889	0.4565
72	1.3840	0.8283	1.0989	1.1454	−1.9442	−0.2624	0.4652
73	1.3489	0.8308	1.1052	1.1475	−1.9052	−0.2366	0.4737
74	1.3159	0.8335	1.1115	1.1496	−1.8672	−0.2114	0.4819
75	1.2851	0.8363	1.1177	1.1516	−1.8302	−0.1869	0.4900
76	1.2562	0.8392	1.1239	1.1536	−1.7942	−0.1630	0.4978
77	1.2290	0.8423	1.1300	1.1555	−1.7590	−0.1396	0.5055
78	1.2035	0.8454	1.1361	1.1574	−1.7246	−0.1169	0.5129
79	1.1795	0.8487	1.1421	1.1592	−1.6911	−0.0946	0.5202
80	1.1569	0.8520	1.1481	1.1610	−1.6584	−0.0729	0.5273
81	1.1357	0.8555	1.1539	1.1627	−1.6265	−0.0517	0.5342
82	1.1156	0.8590	1.1598	1.1644	−1.5953	−0.0310	0.5410
83	1.0967	0.8626	1.1655	1.1661	−1.5648	−0.0108	0.5475
84	1.0789	0.8663	1.1712	1.1677	−1.5349	0.0090	0.5540
85	1.0620	0.8700	1.1768	1.1693	−1.5057	0.0284	0.5603
86	1.0461	0.8738	1.1824	1.1709	−1.4772	0.0473	0.5664
87	1.0311	0.8777	1.1879	1.1724	−1.4492	0.0658	0.5724
88	1.0168	0.8816	1.1934	1.1739	−1.4219	0.0839	0.5783
89	1.0034	0.8855	1.1987	1.1754	−1.3951	0.1016	0.5840
90	0.9907	0.8896	1.2041	1.1768	−1.3688	0.1189	0.5896
91	0.9786	0.8936	1.2093	1.1782	−1.3431	0.1359	0.5950
92	0.9672	0.8977	1.2145	1.1796	−1.3179	0.1525	0.6004
93	0.9564	0.9018	1.2196	1.1809	−1.2932	0.1688	0.6056
94	0.9461	0.9060	1.2247	1.1822	−1.2690	0.1847	0.6108
95	0.9364	0.9101	1.2297	1.1835	−1.2452	0.2003	0.6158
96	0.9272	0.9143	1.2347	1.1848	−1.2218	0.2156	0.6207
97	0.9185	0.9186	1.2396	1.1860	−1.1989	0.2306	0.6255
98	0.9103	0.9228	1.2444	1.1873	−1.1764	0.2453	0.6302
99	0.9024	0.9271	1.2492	1.1884	−1.1544	0.2597	0.6348
100	0.8950	0.9314	1.2539	1.1896	−1.1327	0.2739	0.6393

TABLE 7

λ^{-2} EMISSIVITY, HIGH TEMPERATURES

T (K)	K_{12}	K_{25}	K_{60}	K_{100}	$log(S_{12}/S_{25})$	$log(S_{25}/S_{60})$	$log(S_{60}/S_{100})$
110	0.8396	0.9748	1.2981	1.2001	−0.9350	0.4014	0.6798
120	0.8089	1.0180	1.3371	1.2089	−0.7662	0.5079	0.7133
130	0.7944	1.0603	1.3718	1.2163	−0.6197	0.5981	0.7414
140	0.7912	1.1009	1.4025	1.2227	−0.4909	0.6753	0.7653
150	0.7958	1.1397	1.4300	1.2282	−0.3767	0.7419	0.7858
160	0.8063	1.1764	1.4546	1.2330	−0.2745	0.7999	0.8036
170	0.8209	1.2110	1.4766	1.2372	−0.1825	0.8507	0.8192
180	0.8388	1.2436	1.4966	1.2409	−0.0991	0.8957	0.8329
190	0.8590	1.2742	1.5146	1.2442	−0.0234	0.9356	0.8451
200	0.8809	1.3029	1.5311	1.2472	0.0459	0.9713	0.8559
210	0.9041	1.3298	1.5460	1.2499	0.1093	1.0033	0.8657
220	0.9282	1.3550	1.5597	1.2523	0.1676	1.0322	0.8745
230	0.9529	1.3786	1.5723	1.2545	0.2214	1.0584	0.8825
240	0.9780	1.4008	1.5839	1.2566	0.2710	1.0822	0.8897
250	1.0032	1.4217	1.5946	1.2584	0.3171	1.1039	0.8964
260	1.0284	1.4412	1.6046	1.2601	0.3598	1.1238	0.9025
270	1.0536	1.4596	1.6138	1.2617	0.3996	1.1421	0.9081
280	1.0785	1.4770	1.6223	1.2632	0.4367	1.1590	0.9133
290	1.1031	1.4933	1.6303	1.2645	0.4713	1.1746	0.9181
300	1.1274	1.5087	1.6378	1.2658	0.5038	1.1890	0.9225
310	1.1513	1.5232	1.6448	1.2670	0.5341	1.2024	0.9267
320	1.1747	1.5370	1.6514	1.2681	0.5626	1.2149	0.9305
330	1.1977	1.5500	1.6576	1.2691	0.5894	1.2266	0.9342
340	1.2202	1.5623	1.6634	1.2701	0.6147	1.2375	0.9376
350	1.2422	1.5740	1.6689	1.2710	0.6385	1.2477	0.9408
360	1.2636	1.5851	1.6741	1.2719	0.6609	1.2573	0.9438
370	1.2846	1.5957	1.6790	1.2727	0.6821	1.2663	0.9466
380	1.3050	1.6057	1.6837	1.2734	0.7022	1.2748	0.9493
390	1.3249	1.6152	1.6881	1.2742	0.7213	1.2829	0.9518
400	1.3443	1.6243	1.6923	1.2749	0.7393	1.2904	0.9542
410	1.3632	1.6330	1.6963	1.2755	0.7564	1.2976	0.9564
420	1.3815	1.6413	1.7001	1.2762	0.7727	1.3044	0.9586
430	1.3994	1.6492	1.7037	1.2767	0.7882	1.3109	0.9607
440	1.4168	1.6568	1.7071	1.2773	0.8030	1.3170	0.9626
450	1.4337	1.6640	1.7104	1.2779	0.8171	1.3228	0.9645
460	1.4502	1.6709	1.7136	1.2784	0.8305	1.3284	0.9662
470	1.4662	1.6776	1.7166	1.2789	0.8433	1.3336	0.9679
480	1.4817	1.6840	1.7195	1.2793	0.8555	1.3387	0.9695
490	1.4968	1.6901	1.7223	1.2798	0.8673	1.3435	0.9711
500	1.5116	1.6960	1.7250	1.2802	0.8785	1.3481	0.9726
510	1.5259	1.7016	1.7275	1.2806	0.8892	1.3525	0.9740
520	1.5398	1.7071	1.7300	1.2810	0.8995	1.3568	0.9754
530	1.5533	1.7123	1.7324	1.2814	0.9094	1.3608	0.9767
540	1.5665	1.7174	1.7347	1.2818	0.9189	1.3647	0.9779
550	1.5793	1.7222	1.7368	1.2822	0.9281	1.3684	0.9791
560	1.5918	1.7269	1.7390	1.2825	0.9368	1.3720	0.9803
570	1.6039	1.7314	1.7410	1.2828	0.9453	1.3755	0.9814
580	1.6157	1.7358	1.7430	1.2832	0.9534	1.3788	0.9825
590	1.6272	1.7400	1.7449	1.2835	0.9612	1.3820	0.9836
600	1.6384	1.7441	1.7467	1.2838	0.9688	1.3851	0.9846
610	1.6494	1.7481	1.7485	1.2841	0.9760	1.3880	0.9855
620	1.6600	1.7519	1.7502	1.2843	0.9831	1.3909	0.9865
630	1.6703	1.7556	1.7519	1.2846	0.9898	1.3937	0.9874
640	1.6804	1.7592	1.7535	1.2849	0.9964	1.3963	0.9883
650	1.6902	1.7626	1.7551	1.2851	1.0027	1.3989	0.9891
660	1.6998	1.7660	1.7566	1.2854	1.0088	1.4014	0.9900
670	1.7092	1.7693	1.7581	1.2856	1.0147	1.4038	0.9908
680	1.7183	1.7724	1.7595	1.2858	1.0205	1.4062	0.9915
690	1.7271	1.7755	1.7609	1.2861	1.0260	1.4084	0.9923
700	1.7358	1.7785	1.7622	1.2863	1.0314	1.4106	0.9930
710	1.7443	1.7814	1.7635	1.2865	1.0366	1.4128	0.9937
720	1.7525	1.7842	1.7648	1.2867	1.0416	1.4148	0.9944
730	1.7606	1.7869	1.7660	1.2869	1.0465	1.4168	0.9951
740	1.7684	1.7896	1.7672	1.2871	1.0513	1.4188	0.9957
750	1.7761	1.7922	1.7684	1.2873	1.0559	1.4207	0.9963
760	1.7836	1.7947	1.7695	1.2875	1.0604	1.4225	0.9970
770	1.7909	1.7971	1.7706	1.2876	1.0647	1.4243	0.9976
780	1.7981	1.7995	1.7717	1.2878	1.0690	1.4260	0.9981
790	1.8051	1.8019	1.7728	1.2880	1.0731	1.4277	0.9987
800	1.8119	1.8041	1.7738	1.2881	1.0771	1.4294	0.9993
810	1.8186	1.8063	1.7748	1.2883	1.0810	1.4310	0.9998
820	1.8252	1.8085	1.7758	1.2885	1.0848	1.4325	1.0003
830	1.8316	1.8106	1.7767	1.2886	1.0885	1.4341	1.0008
840	1.8378	1.8126	1.7776	1.2888	1.0920	1.4355	1.0013
850	1.8440	1.8146	1.7785	1.2889	1.0955	1.4370	1.0018
860	1.8499	1.8166	1.7794	1.2891	1.0990	1.4384	1.0023
870	1.8558	1.8185	1.7803	1.2892	1.1023	1.4398	1.0027
880	1.8615	1.8204	1.7811	1.2893	1.1055	1.4411	1.0032
890	1.8672	1.8222	1.7819	1.2895	1.1087	1.4424	1.0036
900	1.8727	1.8240	1.7828	1.2896	1.1118	1.4437	1.0041
910	1.8781	1.8257	1.7835	1.2897	1.1148	1.4449	1.0045
920	1.8833	1.8274	1.7843	1.2898	1.1177	1.4461	1.0049
930	1.8885	1.8291	1.7851	1.2900	1.1206	1.4473	1.0053
940	1.8936	1.8307	1.7858	1.2901	1.1234	1.4485	1.0057
950	1.8986	1.8323	1.7865	1.2902	1.1261	1.4496	1.0061
960	1.9034	1.8339	1.7872	1.2903	1.1288	1.4507	1.0065
970	1.9082	1.8354	1.7879	1.2904	1.1314	1.4518	1.0068
980	1.9129	1.8369	1.7886	1.2905	1.1340	1.4529	1.0072
990	1.9175	1.8383	1.7893	1.2906	1.1365	1.4539	1.0075
1000	1.9220	1.8398	1.7899	1.2907	1.1389	1.4549	1.0079

REFERENCES

Beichman, C. A., *et al.* 1984, *Ap. J. (Letters)*, **278,** L45.
Beichman, C. A., Myers, P. C., Emerson, J. P., Harris, S., Mathieu, R., Benson, P. J., and Jennings, R. E. 1986, *Ap. J.*, **307,** 337.
Beichman, C. A., Wilson, R. E., and Goldsmith, P. F. 1988, *Ap. J. (Letters)*, **332,** L81.
Benson, P. J., Myers, P. C., and Wright, E. L. 1984, *Ap. J. (Letters)*, **279,** L27.
Blitz, L., Bazell, D., and Désert, F. X. 1990, *Ap. J. (Letters)*, **352,** L13.
Bloemen, H. 1988, in *Molecular Clouds in the Milky Way and External Galaxies,* ed. R. Dickman, R. Snell, and J. Young (New York: Springer), p. 71.
Boss, A. P. 1989, *Pub. A.S.P.*, **101,** 767.
Boulanger, F., Baud, B., and van Albada, G. D. 1985, *Astr. Ap.*, **144,** L9.
Boulanger, F., and Perault, M. 1988, *Ap. J.*, **320,** 964.
Clemens, D. P. 1985, *Ap. J.*, **295,** 422.
Clemens, D. P., and Barvainis, R. 1988, *Ap. J. Suppl.*, **68,** 257 (CB).
Clemens, D. P., Sanders, D. B., and Scoville, N. Z. 1988, *Ap. J.*, **327,** 139 (CSS).
Dickman, R. L. 1978, *Ap. J. Suppl.*, **37,** 407.
———. 1988, in *Molecular Clouds in the Milky Way and External Galaxies,* ed. R. Dickman, R. Snell, and J. Young (New York: Springer), p. 55.
Dickman, R. L., and Clemens, D. P. 1983, *Ap. J.*, **271,** 143.
Draine, B. T., and Lee, H. M. 1984, *Ap. J.*, **285,** 89.
Fitzgerald, M. P., Stephan, T. C., and Witt, A. N. 1976, *Ap. J.*, **208,** 709.
Goldsmith, P. F., and Langer, W. D. 1978, *Ap. J.*, **222,** 881.
Heyer, M. H., Snell, R. L., Morgan, J., and Schloerb, F. P. 1989, *Ap. J.*, **346,** 220.
Keene, J., Davidson, J. A., Harper, D. A., Hildebrand, R. H., Jaffe, D. T., Lowenstein, R. F., Low, F. J., and Pernic, R. 1983, *Ap. J. (Letters)*, **274,** L43.
Keene, J., Harper, D. A., Hildebrand, R. H., and Whitcomb, S. E. 1980, *Ap. J. (Letters)*, **240,** L43.
Kwan, J., and Valdes, F. 1987, *Ap. J.*, **315,** 92.
Lee, M. H., and Rogers, C. 1987, *Ap. J.*, **317,** 197.
Leung, C. M. 1975, *Ap. J.*, **199,** 340.
———. 1985, in *Protostars and Planets II,* ed. D. Black and M. Mathews (Tucson: University of Arizona Press), p. 104.
Leung, C. M., Kutner, M. L., and Mead, K. N. 1982, *Ap. J.*, **262,** 583.
Liszt, H. S. 1982, *Ap. J.*, **262,** 198.
Magnani, L., Blitz, L., and Mundy, L. 1985, *Ap. J.*, **295,** 402.
Mathis, J. S., Rumpl, W., and Nordsieck, K. H. 1977, *Ap. J.*, **217,** 425.
Mooney, T. J., and Solomon, P. M. 1988, *Ap. J. (Letters)*, **334,** L51.
Myers, P. C. 1983, *Ap. J.*, **270,** 105.
Myers, P. C., Fuller, G. A., Mathieu, R. D., Beichman, C. A., Benson, P. J., Schild, R. E., and Emerson, J. P. 1987, *Ap. J.*, **319,** 340.
Neugebauer, G., *et al.* 1984, *Ap. J. (Letters)*, **278,** L1.
Puget, J. L., and Léger, A. 1989, *Ann. Rev. Astr. Ap.*, **27,** 161.
Schwartz, P. R., Cheung, A. C., Bologna, J. M., Chui, M. F., Waak, J. A., and Matsakis, D. 1977, *Ap. J.*, **218,** 671.
Scoville, N. Z., and Good, J. C. 1987, in *Star Formation in Galaxies,* ed. C. J. L. Persson, NASA CP 2466, p. 3.
Scoville, N. Z., and Solomon, P. M. 1975, *Ap. J. (Letters)*, **199,** L105.
Snell, R. L., Heyer, M. H., and Schloerb, F. P. 1989, *Ap. J.*, **337,** 739.
Snell, R. L., Mundy, L. G., Goldsmith, P. F., Evans, N. J., and Erikson, N. R. 1984, *Ap. J.*, **276,** 625.
Sodrosky, T. J. 1988, Ph.D. thesis, University of Maryland.
Villere, K. R., and Black, D. C. 1980, *Ap. J.*, **236,** 192.
Witt, A. N., and Lillie, C. F. 1973, *Astr. Ap.*, **25,** 397.
Witt, A. N., Oliveri, M. V., and Schild, R. E. 1990, *A.J.*, **99,** 888.
Weiland, J. L., Blitz, L., Dwek, E., Hauser, M. G., Magnani, L., and Rickard, L. J. 1986, *Ap. J. (Letters)*, **306,** L101.
Wood, D. O., and Churchwell, E. 1989, *Ap. J.*, **340,** 265.

DAN P. CLEMENS and JOÃO LIN YUN: Boston University, Astronomy Department, 725 Commonwealth Avenue, Boston, MA 02215

MARK H. HEYER: Five College Radio Observatory, 619I Lederle Graduate Research Center, University of Massachusetts, Amherst, MA 01003